Novel Performance Enhancement Method by Mesoscale-Structure Control of Electrode–Electrolyte Interface in Solid Oxide Fuel Cells

Akio KONNO

2011

Contents

3 Novel cell performance enhancement method by mesoscale-structure control in SOFCs   42

4 A corrugated mesoscale structure on electrode–electrolyte interface for enhancing cell performance in anode-supported SOFC 69

5 Conclusions 90

Nomenclature 94

Acknowledgments

Chapter 1

Introduction

1.1 Background

Fuel cells convert chemical energy of fuels into electrical energy. Among several types solid oxide fuel cells (SOFCs) are drawing attention for their high electricity generation efficiency. A typical SOFC uses an oxide-ion conductive ceramic material as its electrolyte. Because the ceramic electrolyte shows sufficiently high ion conductivity only at high temperature, the SOFC is operated at 600–1000 °C.

Such high operating temperature provides interesting advantages to the SOFC. For example, it dose not need an expensive platinum catalyst that is typically required for low-temperature fuel cells to enhance the electrochemical reaction. It offers possibilities for recovering thermal energy. In addition, its operating temperature makes it suitable for steam reforming reactions of hydrocarbon fuels. By using the heat generated in the SOFC, the endothermic reforming reaction, called the "internal" reforming process, can effectively proceed.

Combining these advantages, unique systems with very high power generation efficiencies can be designed. One example is a town gas-fuelled combined heat and power

(CHP) system tested by Osaka Gas Co., Ltd., & Kyocera Co. In 2006, the CHP system was equipped with a 1 kW class SOFC module and 49% AC electric generation with a 34% heat recovery efficiency was achieved [1]. Another example is a system hybridized with gas turbines (GT). A SOFC–GT hybrid system is known for its high theoretical efficiency, and intensive R&D works can be found in literature. Costamagna et al. performed a system analysis of a 300 kW SOFC–GT hybrid system and reported that it can attain an electricity generation efficiency of over 60% at design point and always over 50% at part load conditions [2]. Both are examples of systems that cannot be achieved with conventional design heat engines, only.

An SOFC is regarded as one of the most promising high-efficient energy conversion devices. Like other new devices under development, however, today's SOFCs have drawbacks. Durability improvement and cost reduction are the major issues that need to be addressed before commercialization. In addition, SOFC ceramic materials usually contain rare-earth elements. Reducing the amount of rare-earth elements is important owing to limited supply and cost. A possible approach toward cost and material reduction is increase of the power density, which is the main objective of this study. Increased power density reduces stack size, weight, heat capacity and cost.

Material improvement is important in SOFC development; there is always a possibility that a new material will further strengthen the advantages of SOFC and overcome the drawbacks. This study focuses on another important direction of the SOFC development: structure control. Several investigations on enhancing power density focus on structure control. In this study, those investigations are classified into three categories depending on the characteristic length of the control structure.

The first category is a "macroscale" approach, which corresponds to the design modification of the cell geometry. The order of its structure control is generally over 1 mm. In a tubular cell design, for example, the surface area density can be improved by reducing the tube diameter. Kendall and Palin [3], Sammes et al. [4], and Suzuki et al. [5] examined "micro-tubular" cells whose diameters are in the range of 1−10 mm. Kendall and Palin

2

demonstrated the power generation of a 2 mm diameter micro-tubular cell [3]. Sammes et al. fabricated and tested a 10 mm micro-tubular cell and designed a 100 W stack [4]. Suzuki et al. reported that a micro-tubular cell of 0.8 mm diameter generates a power density of 0.35 W/cm^2 under 550 °C [5]. A review of the micro-tubular SOFC is presented by Howe et al. [6]. A flat-tubular cell was designed by Siemens Westinghouse to increase the surface area and resulting power density [7]. Lu et al. numerically investigated the flat-tubular cell and reported the flow, gas concentration and temperature fields [8]. In a planar cell design, the power density is generally higher than in standard tubular cells. A monolithic layer built (MOLB)-type cell can further improve surface area density by forming a wavy shape. An early study of the MOLB-type cell was conducted at the Argonne national laboratory [9]. Sakaki et al. reported continuous power generation tests of over 2000 h in 5 kW class MOLB-type module [10]. Yang et al. numerically investigated MOLB-type cells to discuss distributions of temperature, gas concentrations and current density [11]. They compared the performance of the MOLB-type cell with that of a standard planar cell, and reported that the MOLB-type cell produced less uniform current but higher average current density. The power density enhancement by the macroscale approach is essentially an improvement of packaging. A good design increases the cell's surface area in a stack volume. It affects the compactness of the system but its effect on the cost and material reduction is indirect.

The second category is a "microscale" approach. It is widely recognized that the microstructure of porous electrodes has a significant impact on cell performance as well as on cell durability. Therefore, quantification of the porous microstructure and its correlation to cell performance are recent interests [12-15]. The characteristic length is usually smaller than 1 μm. Porous electrodes must have appropriate microstructures that increase the density of reaction sites, reduce resistance to gas transport and establish efficient networks of both ion and electron conductors. Unlike the direct control of structure in the macroscale, the electrode microstructure is usually controlled indirectly and statistically. Sasaki et al. investigated the relationship between lanthanum strontium manganate (LSM) cathode polarization and microstructures that is indirectly controlled by the changing mean particle size of starting

powder, calcination temperature and sintering temperature [16]. Jørgensen et al. investigated the correlation between a cathode polarization, sintering temperature and microstructures in a LSM-yttria stabilized zirconia (YSZ) composite cathode [17]. Haanappel et al. optimized a processing parameter of an LSM-YSZ composite cathode such as mass fraction of the cathode, particle size and influence of calcination of YSZ powder [18]. Nanoscale particles are often used near the electrode–electrolyte interface to increase the number of reaction sites. This forms a multilayer electrode; it is a typical and practical example of a microstructure modification [19]. However, this approach currently encounters durability problems in long-term use [12, 20]. Simwonis et al. measured Ni coarsening of Ni-YSZ and quantified its microstructure from a microscope image [12]. Jørgensen et al. tested the durability of a LSM cathode and reported that degradation ascribed to a microstructural change was observed under current load [20]. A review on the durability of SOFCs is presented by Yokokawa et al [21].

The third category is a "mesoscale", the category addressed in this study. The characteristic length of the mesoscale structure is in the order of 10–100 μm. The thickness control of the electrolyte is a simple example of structure control in this category. At the early stage of SOFC development, electrolyte-supported cells were used. To reduce the ohmic loss at a thick electrolyte, electrode-supported cells were developed. Currently, a typical thickness of the electrolyte in electrode-supported cells is as thin as 10−20 μm. Structure control in this category, however, draws less attention compared to that in the other two categories. Nevertheless, this study focuses on the high potential of structure control for enhancing cell performance. It is worth noting that structure control on this scale has advantages over macroscopic or microscopic scale. Because the structure is large enough compared to the microstructure of the porous electrode, it dose not have durability problem caused by the morphological changes. Moreover, precision fabrication of the designed interface shape is possible. On the other hand, the structure is small enough compared to the macroscopic cell shape that it can be applied to a variety of cell types (e.g., tubular, planar). More importantly, it is possible in principle for the approaches with different geometric characteristic length to be

applied simultaneously and mutually. Hence, an approach with new geometric characteristic length is of great importance.

1.2 Concept of mesoscale structure control

The main objective of this study is to discuss a new concept for enhancing the power density of SOFCs. The proposed concept is based on a two-dimensional structure control of SOFC in the mesoscale range. The theoretical background is explained in this section.

Electrochemical reactions proceed at the three-phase boundary (TPB), where the ion conductor, electron conductor and gas phase meet. TPBs are distributed in the porous electrodes but it is reported that they are not equally active; that is, the electrochemical reactions occur more prominently near the electrode–electrolyte interface [22, 23]. Thus, the most effective thickness of electrodes is an open question; however, in this section, for simplicity, the electrochemical reactions are assumed to take place only at the interface.

Figure 1.1 schematically shows an example of the mesoscale-interface modification applied to the anode–electrolyte interface. If the interface has a wavy shape as shown in Fig. 1.1(b), the interface area is increased compared to that of the flat shape (Fig. 1.1(a)), which implies that the electrochemically active region is enlarged by the wavy shape. At the position

(a) Flat interface   (b) Wavy interface
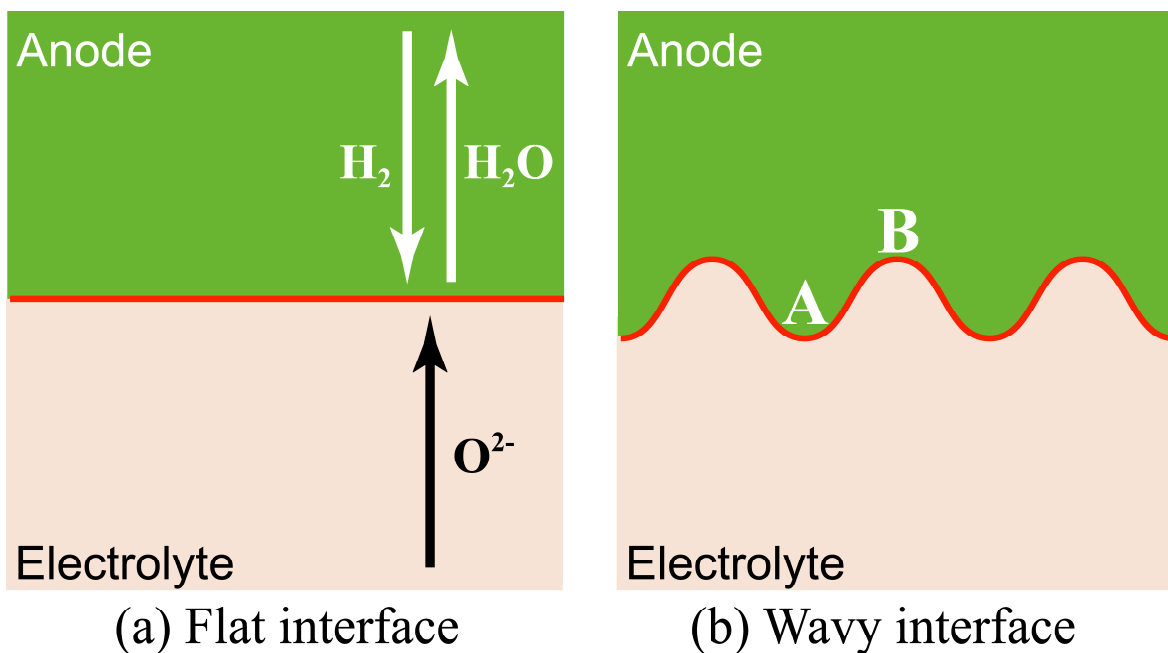
Fig. 1.1 Schematic view of anode–electrolyte interface modification.

marked "A" in Fig. 1.1(b), the electrolyte thickness is reduced with increasing cathode thickness. This implies that the potential loss associated with ion transport in the electrolyte is reduced but the concentration overpotential is increased. At position "B", the opposite situation is obtained. The overall performance of the cell is determined by the sum of all these effects.

We further simplify the problem by neglecting the concentration overpotential because its effect is usually minor in a practical cell operating under normal conditions. Thus, the performance of a flat cell (Fig. 1.1(a)) can be described by the balance between the ion transport resistance in the electrolyte and the reaction resistance at the interface. As a measure of the dominant resistance, we introduce a new dimensionless number, the fuel cell Biot number, defined as follows:

$$Bi_{FC} = \frac{1/ASR_{act}}{\sigma_{ele}/l_{ele}} = \frac{1/ASR_{act}}{1/ASR_{ele}} = \frac{ASR_{ele}}{ASR_{act}} \tag{1-1}$$

ASR, σ_{ele} and l_{ele} are the area-specific resistance, ion conductivity of the electrolyte, and electrolyte thickness, respectively. ASR_{act} can be expressed in terms of the activation overpotential η_{act} and the current density i.

$$ASR_{act} = \frac{\eta_{act}}{i} \tag{1-2}$$

The fuel cell Biot number Bi_{FC} is the ratio of the ion transport resistance of the electrolyte to the reaction resistance and named after Biot number Bi used in the heat transfer field [24]. Table 1.1 compares Bi and Bi_{FC}. Bi_{FC} indicates the dominant resistance that should be reduced to effectively enhance the power generation performance. When Bi_{FC} is larger than unity, ion

Table 1.1 Analogy between heat transfer and SOFC electrochemistry.

	Heat transfer	SOFC
Thickness	l_s [m]	l_{ele} [m]
Conductivity	λ_s [Wm^{-1}K^{-1}]	σ_{ele} [Sm^{-1}]
Inverse of surface resistance	α [Wm^{-2}K^{-1}]	$1/ASR_{act}$ [Sm^{-2}]
Dimensionless number	$Bi = \dfrac{\alpha}{\lambda_s/l_s}$	$Bi_{FC} = \dfrac{1/ASR_{act}}{\sigma_{ele}/l_{ele}}$

transport is the dominant phenomenon, and expansion of the interface area becomes ineffective. Expansion of the interface area can be effective when Bi_{FC} is less than unity, where reaction resistance is the bottleneck. The value of Bi_{FC} is affected by the choice of electrolyte materials, electrolyte thickness, temperature, current density and electrode microstructure.

We assume a conventional cell made of YSZ electrolyte, Ni-YSZ anode and LSM cathode and estimate the values of Bi_{FC}. σ_{ele} and η_{act} are estimated following Bessette *et al*. [25] and Costamagna and Honegger [26], respectively. The values of Bi_{FC} on both anode and cathode sides are shown in Fig. 1.2 for different electrolyte thicknesses and temperatures. The current density is fixed at 300 mA/cm^2. Bi_{FC} can assume values less than 1, especially when the electrolyte is thin. Considering that the electrolyte thicknesses of today's electrode-supported cells are typically in the range of 10−20 μm, Fig. 1.2 indicates the possibility of power density enhancement by shape modification of the electrode–electrolyte interface.

The above discussion by Bi_{FC} is based on the assumption that the electrochemical reactions proceed at the electrode–electrolyte interface. In reality, not only the reaction proceeds at the interface but also the active TPBs distribute in the porous electrode to a few dozen microns from the interface. This is often referred as the "effective thickness" or "active thickness" of the electrode [23, 27]. The effect of concentration overpotential is also neglected. Cell performance is affected by ionic resistivity in the electrolyte, ionic and electronic resistivity in the electrode, electrode reaction resistivity and gas diffusion.

The main objective of this study is to clarify the effectiveness of a mesoscale-structure control of the electrode–electrolyte interface in SOFCs. To consider the effective structure in the mesoscale-interface modification, it is necessary to understand the formation of the active reaction zone of the electrode. In this study, first the effects of transport phenomena in the electrode on the reaction zone are clarified through the results of both a theoretical analysis and a one-dimensional numerical simulation. Because two- or three-dimensional mesoscale structures change transports of electron, oxide ion and gases, as well as the resulting active

reaction zone, the effects of these structures is of particular interest. Two-dimensional numerical simulation is employed in this study. An experimental confirmation of the effectiveness of the mesoscale-interface modification is studied.
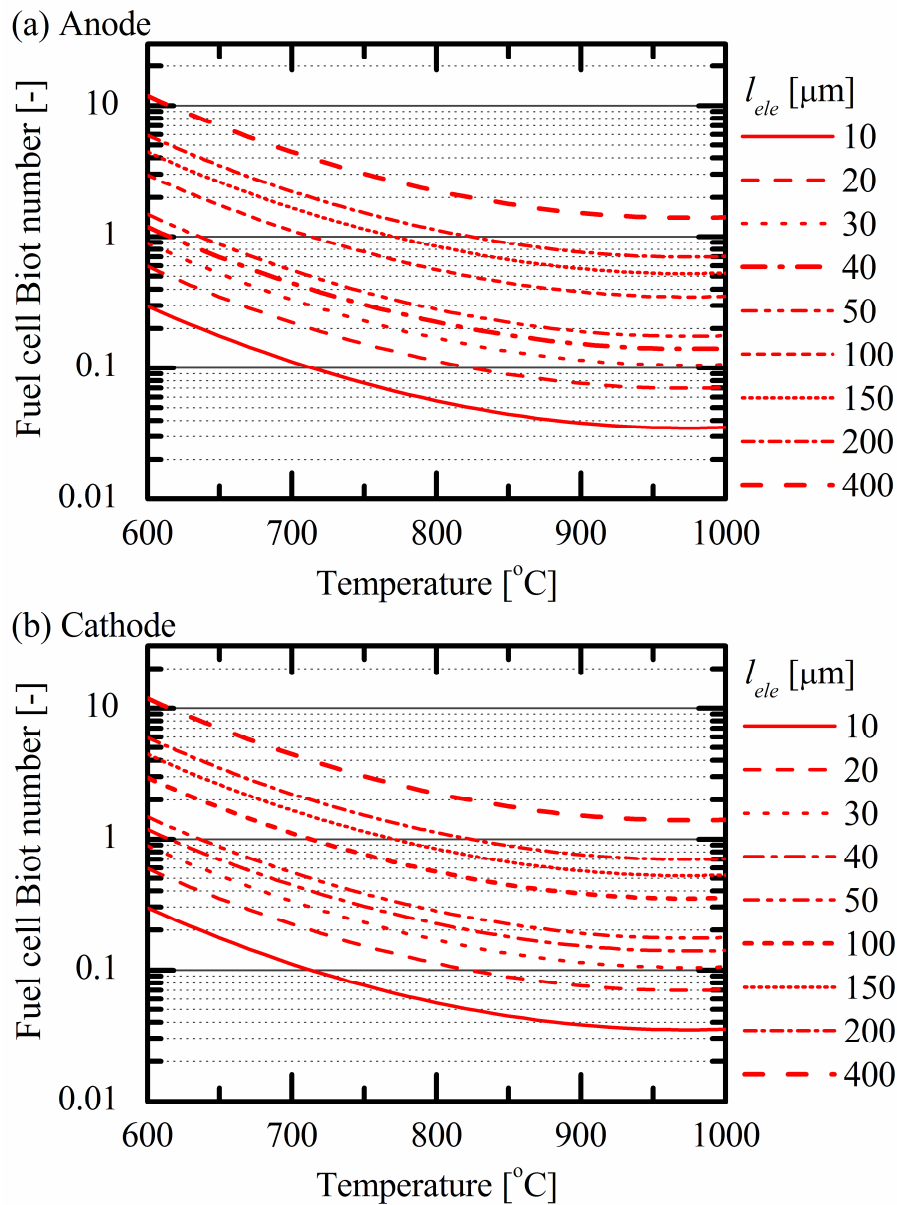
Fig. 1.2 Temperature and electrolyte thickness dependences of fuel cell Biot number at a current density of 300 mA/cm^2.

1.3 Outline of the thesis

Chapter 2 presents the study of the active electrochemical reaction zone. A characteristic length of electron, oxide ion, and gas transport is introduced from these conservation equations and the effect of them on the active reaction zone and electrode performance is discussed through a scale analysis and a one dimensional numerical simulation.

Chapter 3 presents the study of the mesoscale-structure control on the electrode–electrolyte interface. The effect of mesoscale structure and its interface area enlargement on the cell performance is studied numerically and experimentally and discussed.

Chapter 4 presents the study of corrugated mesoscale structure on the both electrode–electrolyte interfaces. The effect of this structure is investigated numerically and discussed about the cell performance and distributions of electric potential, gas concentration, and active reaction zone.

Chapter 5 summarizes the conclusions of this study and offers suggestions for future work.

Reference

[1]   Osaka gas Co., Ltd., http://www.osakagas.co.jp/company/press/pr_2006/060516.html.

[2]   P. Costamagna, L. Magistri, A.F. Massardo, "Design and part-load performance of a hybrid system based on a solid oxide fuel cell reactor and a micro gas turbine", Jounal of Power Sources 96 (2001) 352-368.

[3]   K. Kendall, M. Palin, "A small solid oxide fuel cell demonstrator for microelectronic applications", Journal of Power Sources 71 (1998) 268-270.

[4]   N.M. Sammes, Y. Du, R. Bove, "Design and fabrication of a 100W anode supported micro-tubular SOFC stack", Journal of Power Sources 145 (2005) 428-434.

[5]   T. Suzuki, T. Yamaguchi, Y. Fujishiro, M. Awano, "Fabrication and characterization of micro tubular SOFCs for operation in the intermediate temperature", Journal of Power Sources 160 (2006) 73-77.

[6]   K.S. Howe, G.J. Thompson, K. Kendall, "Micro-tubular solid oxide fuel cell and stacks", Journal of Power Sources 196 (2011) 1677-1686.

[7]   R.A. George, "SECA project at Siemens Westinghouse", Proceedings of the Third Annual Solid State Energy Conversion Alliance (SECA) Workshop, Washington DC (2002).

[8]   Y. Lu, L. Schaefer, P. Li, "Numerical study of a flat-tube high power density solid oxide fuel cell Part I. Heat/mass transfer and fluid flow", Journal of Power Sources 140 (2005) 331-339.

[9]   S. Majumdar, T. Claar, B. Flandermeyer, "Stress and fracture behavior of monolithic fuel cell tapes", Journal of American Ceramic Society 69 (8) (1986) 628-633.

[10] Y. Sakaki, Y. Esaki, M. Hattori, H. Miyamoto, T. Satake, F. Nanjo, T. Matsudaira, K. Takenobu, "Development of 5 kW class MOLB type SOFC", Solid Oxide Fuel Cell V, M. Dokiya, O Yamamoto, H. Tagawa, S. C. Singhal Editors, The Electrochemical Society Proceedings Volume PV97-18 (1995) 61-68.

[11] Y. Yang, G. Wang, H. Zhang, W. Xia, "Computational analysis of thermo-fluid and

electrochemical characteristics of MOLB-type SOFC stacks", Journal of Power Sources 173 (2007) 233-239.

[12] D. Simwonis, F. Tietz, D.Stover, "Nickel coarsening in annealed Ni/8YSZ anode substrates for solid oxide fuel cells", Solid State Ionics 132 (2000) 241-251.

[13] J.R. Wilson, W. Kobsiriphat, R. Mendoza, H.-Y. Chen, J.M. Hiller, D.J. Miller, K. Thornton, P.W. Voorhees, S.B. Adler, S.A. Barnett, "Three-dimensional reconstruction of solid-oxide fuel-cell anode", Nature Materials 5 (2006) 541-544.

[14] J.R. Smith, A. Chen, D. Gostovic, D. Hickey, D. Kundinger, K.L. Duncan, R.T. DeHoff, K.S. Jones, E.D. Wachsman, "Evaluation of the relationship between cathode microstructure and electrochemical behavior for SOFCs", Journal of Power Sources 180 (2009) 90-98.

[15] H. Iwai, N. Shikazono, T. Matsui, H. Teshima, M. Kishimoto, R. Kishida, D. Hayashi, K. Matsuzaki, D. Kanno, M. Saito, H. Muroyama, K. Eguchi, N. Kasagi, H. Yoshida, "Quantification of SOFC anode microstructure based on dual beam FIB-SEM technique", Journal of Power Sources 195 (2009) 955-961.

[16] K. Sasaki, J.-P. Wurth, R. Gschwend, M. Gödickemeier, L.J. Gauckler, "Microstructure -property relations of solid oxide fuel cell cathodes and current collectors", Journal of the Electrochemical Society 143 (2) (1996) 530-543.

[17] M.J. Jørgensen, S. Primdahl, C. Bagger, M. Mogensen, "Effect of sintering temperature on microstructure and performance of LSM-YSZ composite cathodes", Solid State Ionics 139 (2001) 1-11.

[18] V.A.C. Haanappel, J. Mertens, D. Rutenbeck, C. Tropartz, W. Herzhof, D. Sebold, F. Tietz, "Optimisation of processing and microstructural parameters of LSM cathodes to improve the electrochemical performance of anode-supported SOFCs", Journal of Power Sources 141 (2005) 216-226.

[19] E.P. Murray, T. Tsai, S.A. Barnett, "Oxygen transfer process in (La,Sr)MnO$_3$/Y$_2$O$_3$-stabilized ZrO$_2$ cathodes: an impedance spectroscopy study", Solid State Ionics 110 (1998) 235-243.

[20] M.J. Jørgensen, P. Holtappels, C.C. Appel, "Durability test of SOFC cathodes", Journal of Applied Electrochemistry 30 (2000) 411-418.

[21] H. Yokokawa, H. Tu, B. Iwanschitz, A. Mai, "Fundamental mechanisms limiting solid oxide fuel cell durability", Journal of Power Sources 182 (2008) 400-412.

[22] S. Sakamoto, H. Taira, H. Takagi, "Effective electrode reaction area of cofired type planar SOFC", DENKI KAGAKU 64 (6) (1996) 609-613.

[23] M. Brown, S. Primdahl, M. Mogensen, "Structure/performance relations for Ni/yttria-stabilized zirconia anodes for solid oxide fuel cells", Journal of Electrochemical Society 147 (2) (2000) 475-485.

[24] J.P. Holman, Heat Transfer 8th edition, McGraw-Hill (1997).

[25] N.F. Bessette II, W.J. Wepfer, J. Winnick, "A mathematical model of a solid oxide fuel cell", Journal of the Electrochemical Society 142 (11) (1995) 3792-3800.

[26] P. Costamagna, K. Honegger, "Modeling of solid oxide heat exchanger integrated stacks and simulation at high fuel utilization", Journal of the Electrochemical Society 145 (11) (1998) 3995-4007.

[27] A. Abudula, M. Ihara, H. Komiyama, K. Yamada, "Oxidation mechanism and effective anode thickness of SOFC for dry methane fuel", Solid State Ionics 86-88 (1996) 1203-1209.

Chapter 2

Evaluation of active reaction zone in electrode of solid oxide fuel cells

2.1 Effective thickness of electrode

A typical porous electrode of an SOFC consists of three phases, namely, the gas diffusion (pore), electron-conducting and ion-conducting phases. The electrochemical reaction takes place at the TPB where these three phases meet. TPBs are distributed throughout the electrode but they are not equally active as electrochemical reaction sites. Because the resistivity of the ion-conducting phase is relatively large, the electrochemical reaction is more prominent near the electrode–electrolyte interface. The zone where the reaction actively proceeds is often referred as the effective zone. The "effective thickness" of the electrode is the thickness of this effective zone measured from the electrode–electrolyte interface.

In the previous chapter the concept of the mesoscale-structure control of the electrode–electrolyte interface was introduced on the assumption that the electrochemical reaction proceeds only at the electrode–electrolyte interface. This is the same a assuming the effective thickness of the electrode is zero. When mesoscale-structure control is applied to a

real application, the relative size of the interface structure to the effective thickness is important. If the mesoscale structure is much smaller than the effective thickness of the electrode, it will be covered in the effective zone. The effect of the interface area enlargement by the structure cannot be significant under such a condition. The characteristic length of the mesoscale structure should be larger than the effective thickness of the electrode. To discuss whether mesoscale-structure control is effective in a real electrode with non-zero effective thickness, we first need to evaluate the effective thickness.

Experimental investigations to determine the effective thickness of electrodes can be found in literature. A typical experimental approach is to evaluate electrode performance at varying the electrode thickness. On the anode side, Abudula et al. reported that the effective thickness of Ni-YSZ was 120 μm under an operating temperature of 1000 °C [1]. Sakamoto et al. reported that the effective thickness of Ni-YSZ (50:50 wt%) was 10 μm under the same operating temperature [2]. Brown et al. reported that the effective thickness of Ni-YSZ (40:60 vol%) was 10 μm for pure hydrogen fuel and 70 μm for methane fuel under the same operating condition [3]. On the cathode side, Sakamoto et al. reported that the effective thickness was larger than 50 μm for LSM-YSZ (3.5 vol%YSZ, 30 vol%Pore) under an operating temperature of 1000 °C [2]. Fukunaga et al. reported that the effective thickness was less than 20 μm for LSM-YSZ composite under an operating temperature of 850 °C [4]. Koyama et al. reported that the effective thickness was about 15μm for a $Sm_{0.5}Sr_{0.5}CoO_3$ cathode under the operating temperature of 800 °C [5]. Thus, there is a wide variation in the reported values of the effective thickness. From the results of these experimental studies, the effective thickness is observed to be sensitive not only to the material but also to the composition, microstructure and operating condition.

In this chapter, the effective thickness of SOFC electrodes is discussed. To generalize the discussion as much as possible, we start our discussion on the basis of the characteristic lengths of the transport processes in the electrodes, followed by a more detailed discussion through the results of a numerical simulation.

2.2 Scale analysis based on characteristic lengths of transports

In this section a scale analysis is performed on the basis of the characteristic lengths evaluated from the transport equations. The characteristic lengths of electron, ion and gas transports in the porous electrode are compared in order to develop a fundamental discussion on the effective zone and its thickness. Conventional electrode materials are assumed to represent a typical SOFC electrode.

2.2.1 Characteristic length

Electron, oxide ion and gas transports take place in SOFC porous electrodes. The characteristic lengths of these transport phenomena are evaluated from the conservation equations. For the electron and oxide ion, the diffusion equations are expressed as follows:

$$\sigma_{el}^{eff}\frac{\partial^2 \phi_{el}}{\partial x^2} = -i_{ct} \tag{2-1}$$

$$\sigma_{io}^{eff}\frac{\partial^2 \phi_{io}}{\partial x^2} = i_{ct} \tag{2-2}$$

where i_{ct} is the volume-specific charge transfer current associated with the electrochemical reaction. For the gas phase, we choose Fick's model for its simplicity [6]. It is based on Bosanquet approximation of diffusivity and is expressed as follows:

$$D_i^{eff}\frac{\partial^2 C_i}{\partial x^2} = \frac{i_{ct}}{nF} \quad or \quad \frac{D_i^{eff}}{R_0 T}\frac{\partial^2 P_i}{\partial x^2} = \frac{i_{ct}}{nF} \tag{2-3}$$

$$D_i^{eff} = \left(\frac{1}{D_{i,m}^{eff}} + \frac{1}{D_{i,K}^{eff}}\right)^{-1} \tag{2-4}$$

$$D_{i,m}^{eff} = \frac{1}{1-X_i}\sum_{j=1,j\neq i}^{n} D_{ij}^{eff}X_j \tag{2-5}$$

$$D_{ij}^{eff} = \frac{\epsilon}{\tau}D_{ij} \quad and \quad D_{i,K}^{eff} = \frac{\epsilon}{\tau}D_{i,K} \tag{2-6}$$

$$D_{i,K} = \frac{d_p}{2} \frac{2}{3} \sqrt{\frac{8R_0 T}{\pi M_i}} \tag{2-7}$$

$$d_p \approx d_h = \frac{4V_s}{S} \frac{\epsilon}{1 - \epsilon} \tag{2-8}$$

where d_p is the mean pore diameter and is assumed to be equal to the hydraulic diameter d_h as Eq. (2-8) [7]. The characteristic lengths are estimated from Eqs. (2-9−2-11) as follows.

$$l_{el} \sim \sqrt{\frac{\sigma_{el}^{eff} \phi_{el}}{i_{ct}}} \tag{2-9}$$

$$l_{io} \sim \sqrt{\frac{\sigma_{io}^{eff} \phi_{io}}{i_{ct}}} \tag{2-10}$$

$$l_{gas} \sim \sqrt{\frac{nFD_i^{eff} C_i}{i_{ct}}} = \sqrt{\frac{nFD_i^{eff} P_i}{R_0 T i_{ct}}} \tag{2-11}$$

Hereafter, the characteristic lengths of electron, ion and gas transports are referred to as the "electron-conducting length", "ion-conducting length" and "gas-diffusion length", respectively. It is shown that the characteristic length is a function of diffusivity in each phase (effective conductivities or gas diffusivities) and reactivity (charge transfer current). The characteristic length increases with increase in diffusivity and decrease in reactivity. The following ratios of the characteristic lengths are defined. The electric potentials of the two solid phases in Eqs. (2-9) and (2-10) are assumed to be constant and in the same order.

$$\frac{l_{el}}{l_{io}} = \sqrt{\frac{\sigma_{el}^{eff} \phi_{el}}{\sigma_{io}^{eff} \phi_{io}}} \approx \sqrt{\frac{\sigma_{el}^{eff}}{\sigma_{io}^{eff}}} \tag{2-12}$$

$$\frac{l_{gas}}{l_{io}} = \sqrt{\frac{nFD_i^{eff} P_i}{R_0 T \sigma_{io}^{eff} \phi_{io}}} \tag{2-13}$$

These ratios depend on the operating temperature, partial pressure, effective electron and ion conductivities and effective gas diffusivity. Table 2.1 shows the electrode materials we assume in this scale analysis. They are conventional materials for SOFC electrodes. LSM is known to be a mixed ionic and electronic conducting material but its electron conductivity is negligibly small under the oxygen partial pressure of a standard SOFC [8, 9]. Hence, LSM

Table 2.1 Electrode materials in scale analysis.

Electrode	Electron-conducting material	Ion-conducting material
Anode	Ni	YSZ, ScSZ
Cathode	LSM	YSZ, ScSZ

is assumed to be a pure electron-conducting material in this discussion. The electron conductivities for bulk materials of Ni and LSM are given as follows [7, 10, 11]:

$$\sigma_{Ni}^0 = 3.27 \times 10^4 - 10.653T \tag{2-14}$$

$$\sigma_{LSM}^0 = \frac{4.2 \times 10^5}{T} \exp\left(-\frac{1200}{T}\right) \tag{2-15}$$

The ion conductivities for bulk materials of YSZ and scandia-stabilized zirconia (ScSZ) are given as follows [12, 13]:

$$\sigma_{YSZ}^0 = \left(0.00294 \exp\left(\frac{10350}{T}\right)\right)^{-1} \tag{2-16}$$

$$\sigma_{ScSZ}^0 = 104 \exp\left(-\frac{7430}{T}\right) \tag{2-17}$$

The mixing ratio of the electron- and ion-conducting materials in the porous electrode is assumed to be constant at 50:50 vol%. The effective conductivity of each phase depends on the microstructural properties of the electrode, such as volume fraction, tortuosity factor and phase connectivity (percolation probability). Among several models found in literature, we employ the following model. [7].

$$\sigma_i^{eff} = (v_i p_i)^{1.5} \sigma_i^0 \tag{2-18}$$

where subscript i denote electron- or ion-conducting phase, v_i, p_i and σ_i^0 are the volume fraction, percolation probability and conductivity of a bulk material for phase i, respectively. The percolation probability shows the portion of the connected part in the phase of interest. By taking the product of the volume fraction and percolation probability, we can exclude the isolated part that does not contribute to the charge transfer. Assuming a conventional cell, Eq. (2-18) can approximately be written as $\sigma_i^{eff} = 0.1\sigma_i^0$.

2.2.2 Scale analysis based on characteristic lengths

The ratios of the characteristic lengths expressed by Eqs. (2-9) and (2-11) are calculated varying the temperature (600–1000 °C), hydrogen molar fraction on the anode side (5%–99%), oxygen molar fraction on the cathode side (5%–21%) and porosity (0.1–0.8). The values for Ni-YSZ anode, Ni-ScSZ anode, LSM-YSZ cathode and LSM-ScSZ cathode are plotted together in Fig. 2.1. Each area covers a parallelogram region with a 45° slope.

The first discussion focuses on the Ni-YSZ anode. The values of l_{el}/l_{io} and l_{gas}/l_{io} distribute around 10^3 and 10^1–10^2, respectively. Hence, the characteristic lengths of the electron and the gas diffusion are much larger than that of the ion. The hydrogen concentration and the porosity affect the gas-diffusion length. Lowering the hydrogen concentration or porosity reduces the gas-diffusion length but it does not affect ion conduction. The corresponding point in the figure shifts downward along the y-axis as indicated by the blue arrow. The operating temperature affects all three characteristic lengths. When the operating temperature is increased, the corresponding point in the figure shifts in the down-left direction with a 45° slope, as indicated by the red arrow. This is because the temperature dependence of the ion-conducting length is the most prominent among the three characteristic lengths.

When the ion-conducting material is switched to ScSZ, the parallelogram region shifts in the down-left direction compared with the YSZ case. This is caused by the higher ion conductivity of ScSZ compared to that of YSZ. It is also a clue that the value of the ion conductivity has a strong impact in standard electrodes. The value of l_{el}/l_{io} is always greater than 10^2 for both types of anode electrodes. The effect of the electron transport on the active reaction zone is expected to be minor. On the other hand, the gas-diffusion length is comparable to the ion-conducting length depending on the operating condition. Hence gas diffusion may affect the active reaction zone.

A similar trend is observed on the cathode side. However, one main difference from the anode is that the value of l_{el}/l_{io} is approximately one order smaller than that of the anode

19

because of the relatively lower electron conductivity of LSM compared to Ni. Yet the value of l_{el}/l_{io} is still large (10^1–10^2). Thus, the effect of electron transport on the active reaction zone is expected to be minor on the cathode side as well.

In Fig. 2.1, two additional parallelogram frames are shown. These correspond to the cathodes using LSCr as the electron-conductive phase instead of LSM. Although the electron conductivity of LSCr is one order smaller than that of LSM, the electrochemical activity and durability can be improved by replacing LSM with LSCr [14]. In such cases, the effect of electron transport on the active reaction zone is not negligible.
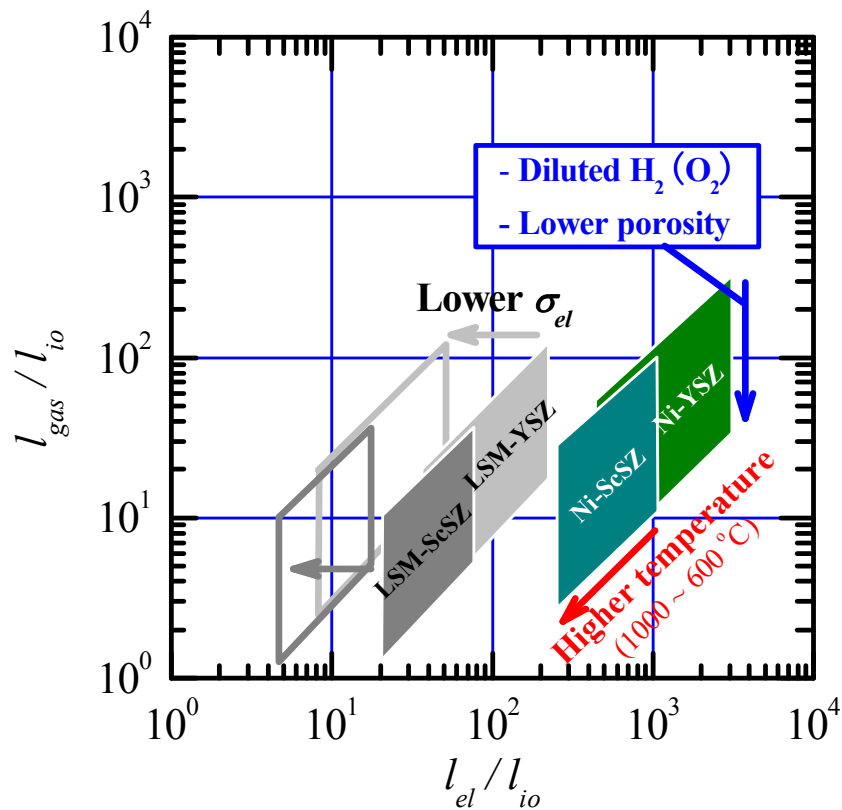
Fig. 2.1 Characteristic length distribution under standard electrode conditions in SOFC.

2.2.3 Characteristic lengths and effective region

In this section, we discuss the active reaction zone in the electrodes using the characteristic lengths introduced in the previous section. As shown in the previous section, the electron-conducting length is sufficiently large in the standard electrodes used today. Therefore, the effects of the ion-conducting and the gas-diffusion lengths are more closely examined.

Figure 2.2 shows the four possible combinations and the resulting active reaction zones when the ion-conducting length l_{io} and the gas-diffusion length l_{gas} are varied. l_{th} is the electrode thickness. Figure 2.2(a) shows the case when l_{io} is shorter than electrode thickness, whereas l_{gas} and l_{el} are longer than l_{th}. The gas and electron supply are enough throughout the electrode thickness. In this case, the electrochemical reaction is limited by the ion supply from the electrolyte and the active reaction zone is expected to exist near the electrode–electrolyte interface. Figure 2.2(b) shows the case when the gas diffusion limits the electrochemical reaction. The active reaction zone is formed near the electrode surface. When both l_{io} and l_{gas} are longer than the electrode thickness, the reaction zone fully expands throughout the electrode as shown in Fig. 2.2(c). If both l_{io} and l_{gas} are shorter than the electrode thickness, the prediction of reaction zone is not straightforward.

From the discussion of scale analysis in the previous section, it is expected that the situations shown in Fig. 2.2(a), (c) and (d) are the typical conditions for a standard cell operating condition.

(a) $l_{io} < l_{th} < l_{el}, l_{gas}$

Electrode surface

l_{io}

l_{el} l_{gas}

$l_{io} \fallingdotseq$ reaction zone

(b) $l_{gas} < l_{th} < l_{el}, l_{io}$

l_{io}

l_{gas}

l_{th}

l_{el}

$l_{gas} \fallingdotseq$ reaction zone

(c) $l_{th} < l_{el}, l_{io}, l_{gas}$

l_{io}

l_{el} l_{gas}

Reaction zone is
fully expanded.

(d) $l_{io}, l_{gas} < l_{th} < l_{el}$

l_{gas}

?

l_{th}

l_{io}

l_{el}

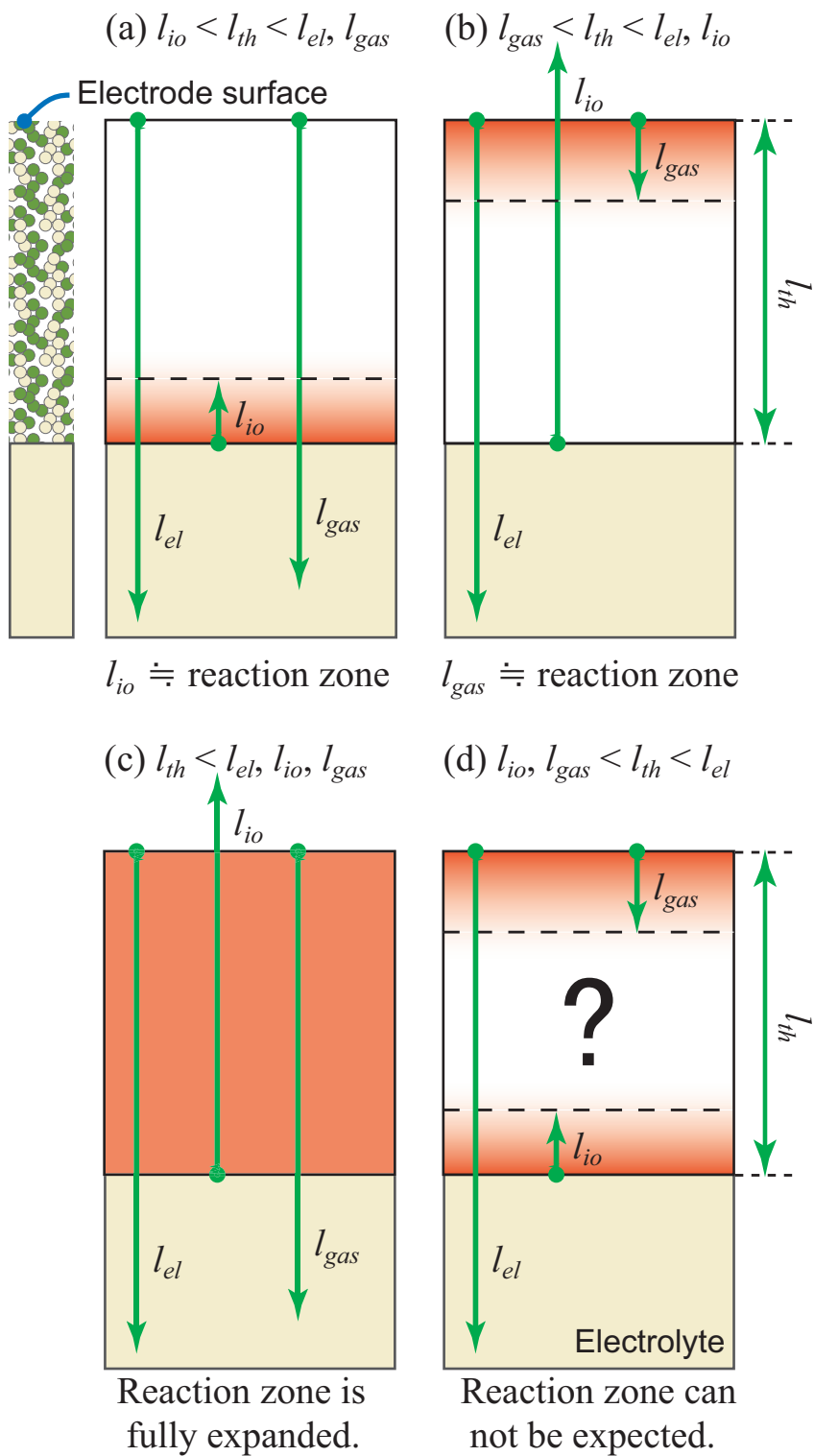Electrolyte

Reaction zone can
not be expected.

Fig. 2.2 Relationships between active reaction zone and characteristic lengths.

2.3 Evaluation of active reaction zone by one-dimensional electrode simulation

By the above discussion based on the characteristic lengths, although an overview of the phenomena in the electrode is obtained, its experimental verification is difficult. To develop a detailed discussion on the electrochemical reaction and transport processes in the electrodes, numerical simulation can be an effective tool. We can find numerical evaluations of the effective electrode thickness in literature. A random-resistor network model [15] considers an electrical circuit model consisting of particles randomly distributed in the electrode. Each particle represents one of the three phases in the electrode and the electric or ionic current distributions in the electrode are simulated. In the micro model [7, 16, 17], macroscopic conservation equations are numerically solved to simulate the electric potentials of the electron- and ion-conducting phases, gas concentration and charge transfer current distribution.

In this study, we adopt the micro model proposed by Nam and Jeon to predict the active reaction zone in the electrode [7]. The distributions of the electric potential, gas concentration and electrochemical reaction rate along the thickness direction are numerically predicted and are compared with the results of the scale analysis.

2.3.1 Simulation method

2.3.1.1 Governing equations

The porous electrodes consist of the electron-conducting, ion-conducting and gas transport phases. Conservation equations of electrons and ions are expressed as follows:

$$\frac{\partial}{\partial x}\left(\sigma_{el}^{eff}\frac{\partial \phi_{el}}{\partial x}\right) = -i_{ct} \tag{2-19}$$

$$\frac{\partial}{\partial x}\left(\sigma_{io}^{eff}\frac{\partial \phi_{io}}{\partial x}\right) = i_{ct} \tag{2-20}$$

where x denotes the thickness direction of the electrode and i_{ct} is the volume-specific charge transfer current explained in the next section.

For the gas phase, the dusty-gas model (DGM) is adopted in the numerical simulation instead of Fick's model adopted in the scale analysis. DGM considers Knudsen diffusion and is capable of modeling the multicomponent system [18−20]. It is written as Eq. (2-21) for each chemical component i of the multicomponent system. The permeability K is estimated from the Carman–Kozeny correlation, given by Eq. (2-22).

$$\frac{N_i}{D_{i,K}^{eff}} + \sum_{j=1,j\neq i}^{n}\frac{X_j N_i - X_i N_j}{D_{ij}^{eff}} = -\frac{P_t}{R_0 T}\nabla X_i - \frac{X_i}{R_0 T}\left(1 + \frac{KP_t}{\mu D_{i,K}^{eff}}\right)\nabla P_t \tag{2-21}$$

$$K = \frac{\epsilon^3}{k_K (1-\epsilon)^2}\left(\frac{V_s}{S}\right)^2 = \frac{\epsilon^3}{k_K (1-\epsilon)^2}\left(\frac{d_{el}}{6}\right)^2 \tag{2-22}$$

For a binary system ($n = 2$), Eq. (2-21) can be separated to find the molar flux of each chemical component. The conservation equations of each chemical component can be rearranged as Eqs. (2-23)–(2-27):

$$\frac{\partial}{\partial x}\left(\frac{k_1}{R_0 T}\frac{\partial P_1}{\partial x}\right) + \frac{\partial}{\partial x}\left(\frac{k_2 P_1}{R_0 T}\frac{\partial P_t}{\partial x}\right) = \frac{i_{ct}}{2F} \tag{2-23}$$

$$\frac{\partial}{\partial x}\left(\frac{k_3}{R_0 T}\frac{\partial P_2}{\partial x}\right) + \frac{\partial}{\partial x}\left(\frac{k_4 P_2}{R_0 T}\frac{\partial P_t}{\partial x}\right) = -\frac{i_{ct}}{2F} \tag{2-24}$$

$$k_1 = \frac{D_{12}^{eff}D_{1,K}^{eff}}{D_{12}^{eff} + D_{m,K}^{eff}} , \quad k_3 = \frac{D_{12}^{eff}D_{2,K}^{eff}}{D_{12}^{eff} + D_{m,K}^{eff}} \tag{2-25}$$

$$k_2 = k_4 = \frac{1}{P_t}\frac{D_{1,K}^{eff}D_{2,K}^{eff}}{D_{12}^{eff} + D_{m,K}^{eff}} + \frac{K}{\mu} \tag{2-26}$$

$$D_{m,K}^{eff} = X_1 D_{2,K}^{eff} + X_2 D_{1,K}^{eff} \tag{2-27}$$

where subscripts 1 and 2 denote H_2 and H_2O on the anode side and O_2 and N_2 on the cathode side, respectively.

2.3.1.2 Electrochemical reaction model

The following electrochemical reactions proceed in the anode and cathode, respectively.

$$H_2 + O^{2-} \rightarrow H_2O + 2e^- \tag{2-28}$$

$$\frac{1}{2}O_2 + 2e^- \rightarrow O^{2-} \tag{2-29}$$

The reactants hydrogen and oxygen are supplied from the gas channel to the porous electrode and are consumed at the TPBs inside the electrodes. The local charge-transfer current is expressed with the Butler–Volmer-type equation as follows:

$$i_{ct} = i_0\left[\exp\left(\frac{\beta nF}{R_0 T}\eta_{act}\right) - \exp\left(\frac{-(1-\beta)nF}{R_0 T}\eta_{act}\right)\right] \tag{2-30}$$

where i_0 is the local exchange current estimated for a unit volume of the electrode (A/m^3). β is the transfer coefficient that is associated with the symmetry of the polarization curve between the anodic and cathodic conditions, and is set at 0.5 [21].

The activation overpotential is modeled on the basis of the local electric potential difference between electron- and ion-conducting phases in the electrode and is defined as a bias from the equilibrium electrode potential at the interface between the electron- and ion-conducting phases as follows.

$$\eta_{act} = E - E^{eq} = \Phi_{el} - \Phi_{io} - E_0^{eq} - \frac{R_0 T}{2F} \ln\left(\frac{P_{H_2O,bulk}}{P_{H_2,bulk}}\right) - \frac{R_0 T}{2F} \ln\left(\frac{P_{H_2,bulk}}{P_{H_2}} \frac{P_{H_2O}}{P_{H_2O,bulk}}\right) \quad (2\text{-}31)$$

E is electric potential difference between electron- and ion-conducting phases. E^{eq} and E_0^{eq} are the equilibrium electrode potential under gas concentrations at a reaction site and the standard equilibrium potential, respectively. Φ_{io} and Φ_{el} are the electric potentials at each phase. Because the third and forth terms of the right hand side of Eq. (2-31) are constant throughout the electrode if we assume an isothermal condition, the electric potentials of the two phases can be rearranged. The potentials ϕ_{el} and ϕ_{io} are introduced as expressed as Eqs. (2-32) and (2-33), and thus Eqs. (2-34) and (2-35) are obtained.

$$\phi_{el} = \Phi_{el} \quad (2\text{-}32)$$

$$\phi_{io} = \Phi_{io} + E_0^{eq} + \frac{R_0 T}{2F} \ln\left(\frac{P_{H_2O,bulk}}{P_{H_2,bulk}}\right) \quad (2\text{-}33)$$

$$\eta_{act} = \phi_{el} - \phi_{io} - \eta_{con} \quad (2\text{-}34)$$

$$\eta_{con} = \frac{R_0 T}{2F} \ln\left(\frac{P_{H_2,bulk}}{P_{H_2}} \frac{P_{H_2O}}{P_{H_2O,bulk}}\right) \quad (2\text{-}35)$$

By these definitions, the electric potential difference between two phases can be described as a sum of the activation and concentration overpotentials. Note that the electric potentials of the electron- and ion-conducting phases (ϕ_{el} and ϕ_{io}) in sections 2.2.1 and 2.3.1 are based on these definitions.

2.3.1.3 Three-phase boundary density and exchange current

To evaluate a local reaction rate, we need to know the local TPB density and an exchange current per TPB length. The exchange current per TPB length is estimated from experiments using patterned electrodes [22]. The inverse of the charge-transfer resistance is linearly proportional to the TPB length.

$$\frac{1}{R_{ct}} = \frac{L_{tpb}}{r_{ct}^L} \tag{2-36}$$

where r_{ct}^L is the charge-transfer resistance per TPB length. If the overpotential is sufficiently low, the Butler–Volmer equation can be approximated by linear form expressed as Eq. (2-35). The charge-transfer current is obtained as Eq. (2-38).

$$I = \frac{I_0 nF}{R_0 T} \eta_{act} \tag{2-37}$$

$$I_0 = \frac{R_0 T}{nF} \frac{I}{\eta_{act}} = \frac{R_0 T}{nF} \frac{1}{R_{ct}} \tag{2-38}$$

Substituting Eq. (2-36) into Eq. (2-38), the exchange current per TPB length i_0^L (A/m) is calculated as follows:

$$\frac{I_0}{L_{tpb}} = i_0^L = \frac{R_0 T}{nF} \frac{1}{r_{ct}^L} \tag{2-39}$$

The local exchange current per volume i_0 (A/m^3) is calculated by taking the product of the exchange current per TPB length i_0^L and TPB density l_{tpb} (m/m^3) as follows:

$$i_0 = i_0^L l_{tpb} \tag{2-40}$$

Eq. (2-40) shows that the exchange current per volume is determined by the catalytic activity at a reaction site and the electrode microstructure.

Table 2.2 shows empirical equations of i_0^L found in literature. There is still a wide discrepancy even for the cases using the same materials (Ni-YSZ). The reason for this

Table 2.2 Empirical equations of exchange current density per TPB length.

	Exchange current density for TPB i_0^L [A/m]	Ref.
Ni-YSZ	$0.0344 P_{H_2}^{0.11} P_{H_2O}^{0.67} \exp\left(-\dfrac{10200}{T}\right)$	[22]
Ni-YSZ	$31.4 P_{H_2}^{-0.03} P_{H_2O}^{0.4} \exp\left(-\dfrac{18300}{T}\right)$	[23, 24]
LSM-YSZ	$1.10 P_{O_2}^{0.5} \exp\left(-\dfrac{16500}{T}\right)$	[25]

discrepancy is not clear and further investigation is needed. In this study, however, $i^L{}_0$ is assumed to be constant at 10^{-4} A/m because the operating temperature and the gas concentration supplied are maintained constant. This value is a moderate value for the calculation condition set in this study. The TPB density is set at 2.5 μm/μm^3, as experimentally evaluated through three-dimensional measurement [26].

2.3.1.4 Calculation conditions

The Ni-YSZ anode is used as an example to discuss the active reaction zone of electrodes. Figure 2.3 shows the simulation model of the anode. It has three grid systems corresponding to the electron-conducting, ion-conducting and the gas transport phases. The governing equations are discretized using the finite-volume method [27] and are solved simultaneously with the electrochemical reaction model.

Table 2.3 summarizes the calculation condition. The electric potential of the ion-conducting phase at the electrode–electrolyte interface is maintained constant at 0 V, while the electric potential of the electron-conducting phase at the anode surface is set at 0.1 V. The difference between these two potentials corresponds to the total electrode overpotential, η_t.

Table 2.3 Calculation conditions.

| Calculation parameter	Value
Temperature T	800 °C
Pressure P_t	0.1013 MPa
Molar fraction of H_2 X_{H_2}	0.9
Molar fraction of H_2O X_{H_2O}	0.1
Exchange current density per TPB length i_0^L	0.0001 A/m
TPB density l_{tpb}	2.5 μm/μm^3
Tortuosity factor τ	3.0
Transfer coefficient β	0.5
Total overpotential η_t	0.1 V
Specific surface of solid phase S/V_s	6×10^6 m^2/m^3
Kozeny constant k_K	5
Electrode thickness l_{th}	50 μm
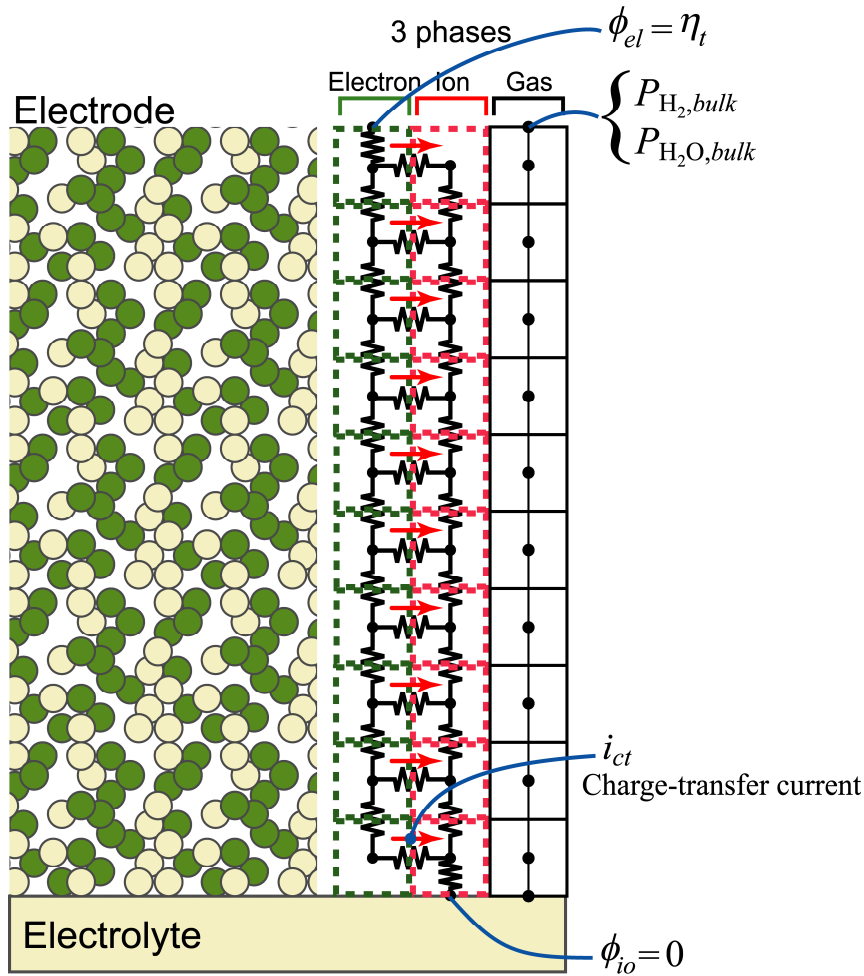
Fig. 2.3 Calculation model of SOFC electrode.

The supplied fuel is a mixture of hydrogen and water vapor and its composition is maintained constant on the anode surface.

Considering the result of the abovementioned scale analysis, the electron-conducting length is assumed to be sufficiently large and the effects of the ion-conducting and gas-diffusion lengths are studied. The effective ion conductivity is varied in the range of 0.0001–0.05 S/cm. It sufficiently covers the range expected in a real application. The gas-diffusion length is indirectly controlled by varying the porosity in the range of 0.1–0.8.

The following assumptions are used for calculating characteristic lengths. To calculate the ion-conducting length, the electric potential in Eq. (2-10), ϕ_{io}, is assumed to be constant at total electrode overpotential. The partial pressure of hydrogen in Eq. (2-11) is set at the value

of supplied gas for estimating the gas-diffusion length. The volume-specific charge transfer current in Eqs. (2-10) and (2-11) is assumed to be the exchange current per unit volume.

2.3.1.5 Evaluation of effective thickness

The effective thickness l_{eff} is defined as the zone measured from the electrode–electrolyte interface where 90% of the total electrochemical reaction takes place.

$$0.9I_t = \int_{l_{th}}^{l_{eff}-l_{th}} i_{ct}dV \tag{2-41}$$

2.3.2 Results and discussion

2.3.2.1 Effect of ion-conducting length

Figure 2.4 shows the electric potential distributions of the electron- and ion-conducting phases in the anode. The origin of the x-coordinate is set at the anode surface and the point at $x = 50$ μm corresponds to the anode–electrolyte interface. The difference between Fig. 2.4(a) and (b) is the ion-conducting length. As the electron-conducting length is sufficiently long, the electric potential in the electron-conducting (Ni) phase, which is denoted by the black solid line in this figure, is uniform at the constant value of 0.1 V. The potential distribution of the ion-conducting phase is indicated by the green solid line. The difference between the black line and the green line corresponds to the activation and concentration overpotentials. They are separately estimated using Eqs. (2-34) and (2-35) and are shown in this figure. Because the gas-diffusion length in these calculations is relatively long (426 μm) compared to the electrode thickness, the concentration overpotential is not significant. The activation overpotential is generally larger than the concentration overpotential. It takes the maximum value at the interface and decreases with the increase of the distance from the interface. Its distribution is, consequently, biased to the anode–electrolyte interface side. The zone with large activation overpotential corresponds well with the zone where the electrochemical reaction is active. The volume-specific charge transfer current is large near the interface as shown in the figure. Comparing Fig. 2.4(a) and (b), the effect of the ion-conducting length is clarified. The active reaction zone biases more prominently to the interface side in case of the shorter ion-conducting length (Fig. 2.4(b), 6.3 μm). The effective thickness is calculated for both cases and is marked in the figure. It is confirmed that the longer ion-conducting length yields a larger reaction zone and effective thickness. These trends found in the simulation results are consistent with the results of the scale analysis. This calculation condition set corresponds to the situation shown in Fig. 2.2(a).

(a) $\varepsilon = 0.3$, $\sigma_{io} = 0.005$ S/cm ($l_{gas} = 426$ μm, $l_{io} = 14$ μm)

(b) $\varepsilon = 0.3$, $\sigma_{io} = 0.001$ S/cm ($l_{gas} = 426$ μm, $l_{io} = 6.3$ μm)
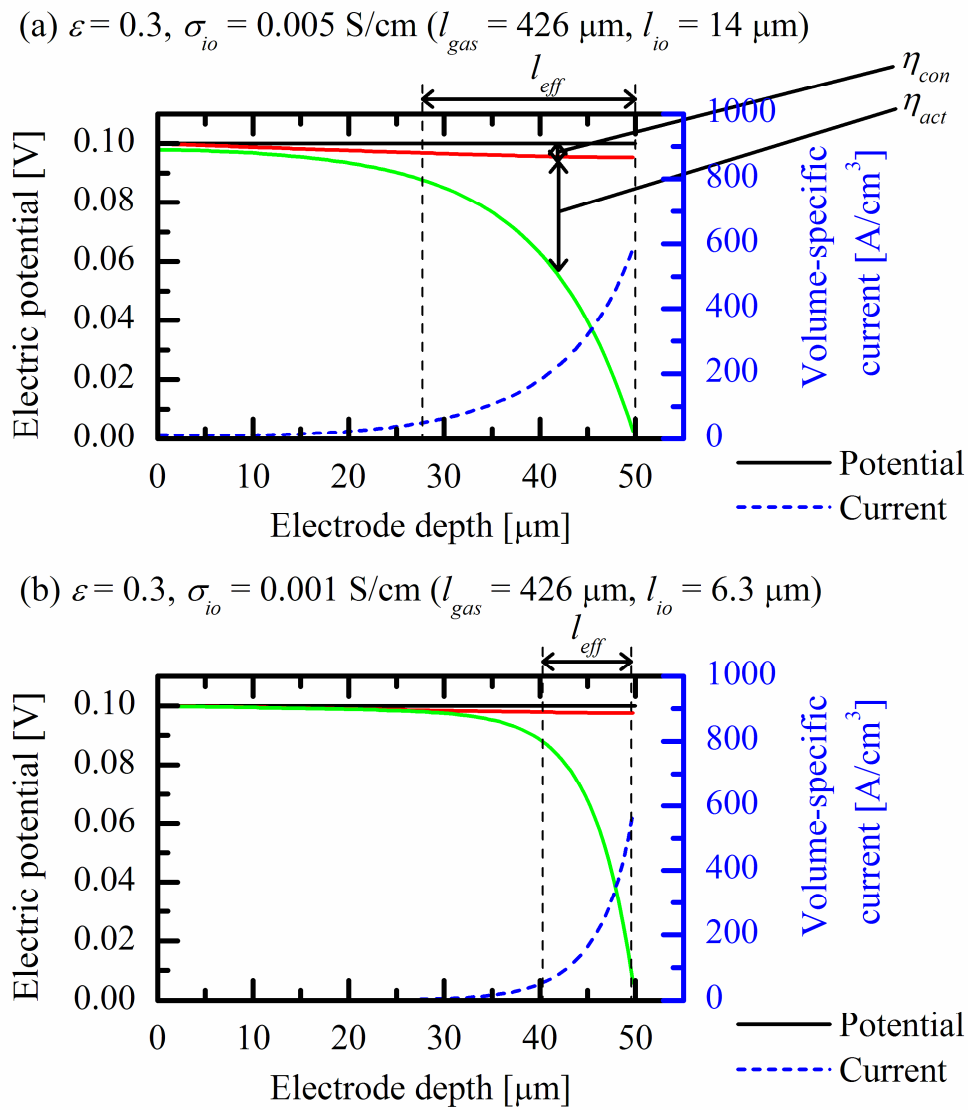
Fig. 2.4 Potential field and volume-specific charge transfer current distribution under large gas-diffusion length.

2.3.2.2 Effect of gas-diffusion length

Figure 2.5 shows the effects of the ion-conducting length and the gas-diffusion length on the average current density. The average current density is evaluated as the electric current obtained for unit anode surface area. Because the total overpotential of the anode is given as the boundary condition and is maintained constant, the average current density can be used as an indicator of anode performance. Figure 2.5 clearly shows that the current density increases with the characteristic lengths. A strong dependency of the average current density on the ion-conducting length is observed. Anode performance is primarily governed by the ion-conducting length but the gas diffusion also affects the performance when the ion-conducting length is long.

Figure 2.6 shows how the ion-conducting length and/or the gas-diffusion length affect the effective thickness of the anode. It shows that the effective thickness of a standard anode is in the order of 10 μm. The relationship between the characteristic lengths and the effective thickness can be explained by the results of the scale analysis shown in Fig. 2.2. When the gas-diffusion length is sufficiently long but the ion-conducting length is short, the effective thickness is proportional to the ion-conducting length. This case corresponds to Fig. 2.2(a). Under this condition, the concentration overpotential can be ignored and the effective thickness is determined by the combined effects of ionic resistance and reaction resistance. If ion conductivity is improved so that the oxygen ion reaches the anode surface, the effective thickness becomes nearly equal to the anode thickness. The active reaction zone covers more than 80% of the anode thickness (50 μm). This situation corresponds to Fig. 2.2(c). In these two cases represented by Fig. 2.2(a) and (c), anode performance improves with increasing effective thickness, as can be confirmed by comparing Figs. 2.5 and 2.6.
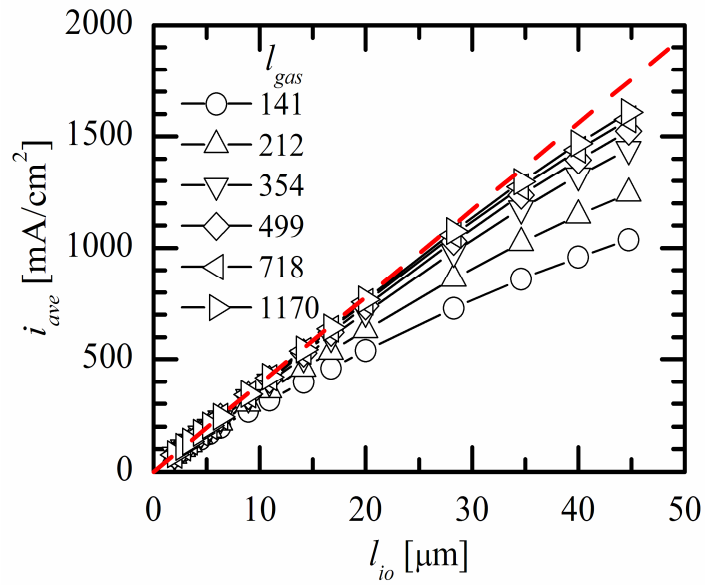
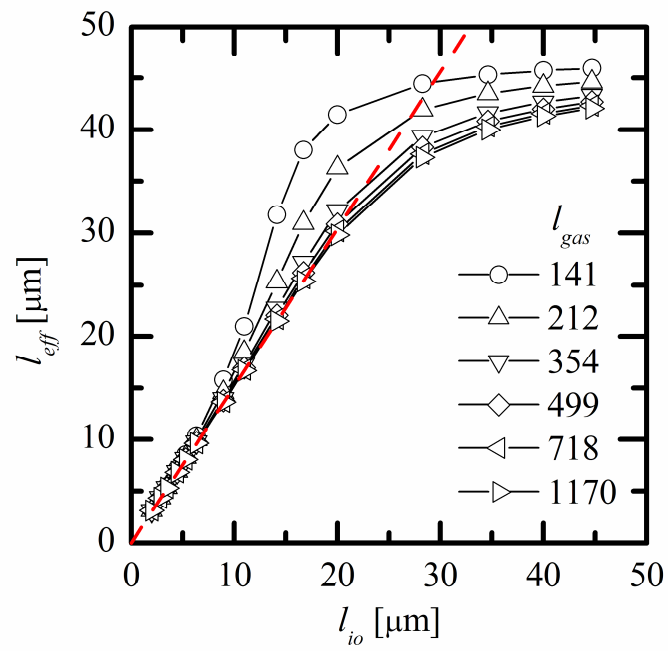Fig. 2.5 Effects of the characteristic lengths on average current density.

Fig. 2.6 Effect of the characteristic lengths on the effective thickness.

On the other hand, it can be seen in Fig. 2.6 that the effective thickness increases with decreasing gas-diffusion length. This situation corresponds to Fig. 2.2(d) and it becomes clearer when the gas-diffusion length is short. However, in this condition, anode performance decreases with increasing effective thickness. When the concentration overpotential is not negligible, the supply of the reactants to the anode–electrolyte interface region is limited. The portion of the active reaction sites increases near the anode surface region where the
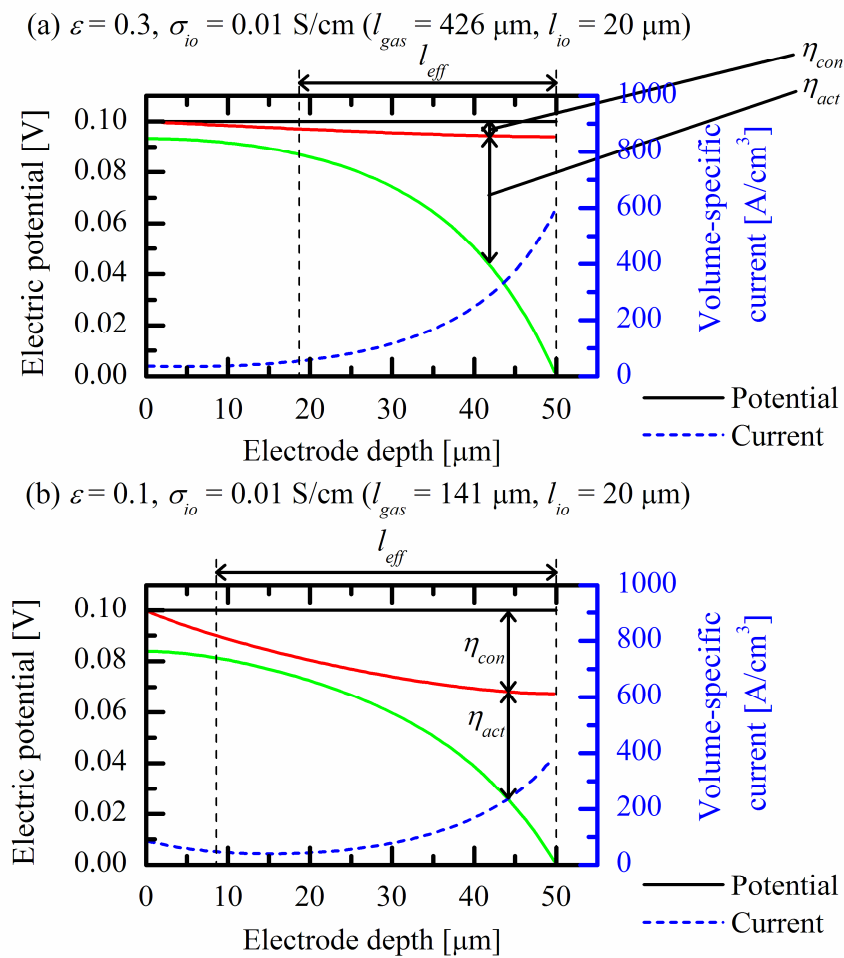

Fig. 2.7 Effect of gas-diffusion length on electrochemical reaction area with large ionic characteristic length ($l_{io} = 20$ μm).

concentration overpotential is negligible. It results in the expansion of the active reaction zone. Because the expansion of the reaction zone causes increase in the ionic resistance, ohmic loss associated with the ion conduction increases. This situation can be clearly observed in Fig. 2.7, which shows the electric potential distributions of the electron- and ion-conducting phases. The difference between Fig. 2.7(a) and (b) is the gas-diffusion length, which is 426 μm and 141 μm, respectively. It can be observed that the concentration overpotential causes almost half of the total overpotential in the case of the shorter gas-diffusion length (141 μm), while the concentration overpotential is almost negligible when the gas-diffusion length is sufficiently long (426 μm). It leads to a difference in the distribution of the charge transfer current that is closely related to the activation overpotential. In both cases, the electrochemical reaction is most active near the anode–electrolyte interface. However, its distribution is relatively flat when the gas-diffusion length is short, thus resulting in a relatively long effective thickness of approximately 41 μm, as shown in Fig. 2.7(b). The expansion of the effective thickness, however, does not necessarily imply an improved performance. The value of the average current density is smaller in the case with the shorter gas-diffusion length, as shown in Fig. 2.5.

2.4 Summary

In this chapter, the active reaction zone of the SOFC porous electrode is discussed. First, a scale analysis was performed based on the characteristic lengths of the electron, ion and gas transports assuming conventional electrode materials. The results of the scale analysis indicate that the characteristic length of the ion transport is the shortest among the three characteristic lengths under typical operating conditions. Hence, the active reaction zone is primarily governed by the ion transport. The electron-conducting length is sufficiently long in a conventional electrode and its effects on the active zone are minor. The gas-diffusion length can be close to the ion-conducting length when the operating temperature is high and the gas diffusivity is low. Under such conditions, the gas diffusion can affect the active reaction zone and electrode performance.

To understand the transport phenomena in the porous electrode of the cell and obtain information on the effective thickness, a one-dimensional numerical simulation was developed and applied to a conventional Ni-YSZ anode. The electric potential distributions of the electron- and ion-conducting phases, activation and concentration overpotentials and charge transfer current were obtained as the simulation results. The obtained results are summarized as follows:

(1) When the gas-diffusion length is sufficiently long, the electrochemical reaction actively proceeds near the electrode–electrolyte interface. The effective thickness is linearly proportional to the ion-conducting length when the ion-conducting length is relatively short. This is expected to be a typical situation in a conventional electrode. The effective thickness is in the order of 10 μm.

(2) When both gas-diffusion and ion-conducting lengths are long compared to the electrode thickness, the active reaction zone covers almost all regions of the electrode. Electrode performance can be improved by increasing the electrode thickness in this case.

(3) When both gas-diffusion and ion-conducting lengths are short, the electrode performance is suppressed. The expansion of the effective thickness observed in this case is only a result of the limited reaction rate near the electrode–electrolyte interface because of the significant concentration overpotential. The portion of the oxygen ion that is forced to move a long distance from the interface increases. Decreasing gas-diffusion length leads to increasing concentration overpotential and the ohmic loss due to ion conduction in the electrode.

The scale analysis using the characteristic lengths cannot predict an accurate reaction zone when the gas-diffusion length is close to the ion-conducting length. However, it is confirmed that the predicted reaction zone by scale analysis agrees with the result of the one-dimensional simulation, when the gas-diffusion length is long. The scale analysis is simple and useful for intuitively understanding the effect of transport phenomena in these phases. The one-dimensional simulation can clarify the effect of gas-diffusion length on electrode performance and active reaction zone.

Reference

[1] A. Abudula, M. Ihara, H. Komiyama, K. Yamada, "Oxidation mechanism and effective anode thickness of SOFC for dry methane fuel", Solid State Ionics 86-88 (1996) 1203-1209.

[2] S. Sakamoto, H. Taira, H. Takagi, "Effective electrode reaction area of cofired type planar SOFC", DENKI KAGAKU 64 (6) (1996) 609-613.

[3] M. Brown, S. Primdahl, M. Mogensen, "Structure/performance relations for Ni/yttria-stabilized zirconia anodes for solid oxide fuel cells", Journal of Electrochemical Society 147 (2) (2000) 475-485.

[4] H. Fukunaga, M. Ishino, K. Yamada, "Effective thickness of Ni-Sm-doped ceria cermet anode for solid oxide fuel cell", Electrochemical and Solid-State Letters 10 (1) (2007) 16-18.

[5] M. Koyama, C. Wen, T. Masuyama, J. Otomo, H. Fukunaga, K. Yamada, K. Eguchi, H. Takahashi, "The mechanism of porous $Sm_{0.5}Sr_{0.5}CoO_3$ cathodes used in solid oxide fuel cells", Journal of Electrochemical Society 148 (7) (2001) 795-801.

[6] J.W. Veldsink, R.M.J. van Damme, G.F. Versteeg, W.P.M. van Swaaij, "The use of the dusty-gas model for the description of mass transport with chemical reaction in porous media", The Chemical Engineering Journal 57 (1995) 115-125.

[7] J.H. Nam, D.H. Jeon, "A comprehensive micro-scale model for transport and reaction in intermediate temperature solid oxide fuel cells", Electrochimica Acta 51 (2006) 3446-3460.

[8] M.J.L. Østergård, M. Mogensen, "*ac* impedance study of the oxygen reduction mechanism on $La_{1-x}Sr_xMnO_3$ in solid oxide fuel cells", Electrochimica Acta 38 (14) (1993) 2015-2020.

[9] I. Yasuda, K. Ogasawara, M. Hishinuma, T. Kawada, M. Dokiya, "Oxygen tracer diffusion coefficient of (La, Sr)$MnO_{3\pm\delta}$", Solid State Ionics 86-88 (1996) 1197-1201.

[10] U. Anselmi-Tamburini, G. Chiodelli, M. Arimondi, F. Maglia, G. Spinolo, Z.A. Munir,

"Electrical properties of Ni/YSZ cermets obtained through combustion synthesis", Solid State Ionics 110 (1998) 35-43.

[11] J.R. Ferguson, J.M. Fiard, R. Herbin, "Three-dimensional numerical simulation for various geometries of solid oxide fuel cells", Journal of the Power Sources 58 (1996) 109-122.

[12] N.F. Bessette II, W.J. Wepfer, J. Winnick, "A mathematical model of a solid oxide fuel cell", Journal of the Electrochemical Society 142 (11) (1995) 3792-3800.

[13] N.Q. Minh, T. Takahashi, Science and technology of ceramic fuel cells, Elsevier (1995).

[14] Y.-J. Yang, T.-L. Wen, H. Tu, D.-Q. Wang, J. Yang, "Characteristics of lanthanum strontium chromite prepared by glycine nitrate process", Solid State Ionics 135 (2000) 475-479.

[15] L.C.R. Schneider, C.L. Martin, Y. Bultel, D. Bouvard, E. Siebert, "Discrete modeling of the electrochemical performance of SOFC electrodes", Electrochimica Acta 52 (2006) 314-324.

[16] P. Costamagna, P. Costa, V. Antonucci, "Micro-modelling of solid oxide fuel cell electrodes", Electrochimica Acta 43 (3-4) (1998) 375-394.

[17] S.H. Chan, Z.T. Xia, "Anode micro model of solid oxide fuel cell", Journal of the Electrochemical Society 148 (4) (2001) 388-394.

[18] E.A. Mason, A.P. Malinauskas, R.B. Evans III, "Flow and diffusion of gases in porous media", The Journal of Chemical Physics 46 (8) (1967) 3199-3216.

[19] D. Arnošt, P. Schneider, "Dynamic transport of multicomponent mixture of gases in porous solids", The Chemical Engineering Journal 51 (1995) 91-99.

[20] R. Suwanwarangkul, E. Croiset, M.W. Fowler, P.L. Douglas, E. Entchev, M.A. Douglas, "Performance comparison of Fick's, dusty-gas and Stefan-Maxwell models to predict the concentration overpotential of a SOFC anode", Journal of Power Sources 122 (2003) 9-18.

[21] C. Berger, Handbook of fuel cell technology, Prentice-Hall (1968).

[22] A. Bieberle, L.P. Meier, L.J. Gauckler, "The electrochemistry of Ni pattern anodes used

as solid oxide fuel cell model electrodes", Journal of the Electrochemical Society 148 (6) (2001) 646-656.

[23] B. de Boer, "SOFC anode: hydrogen oxidation at porous nickel and nickel/yttria-stabilised zirconia cermet electrodes", Ph.D Thesis, University of Twente, Netherlands (1998).

[24] Y. Suzue, N. Shikazono, N. Kasagi, "Micro modeling of solid oxide fuel cell anode based on stochastic reconstruction", Journal of Power Sources 184 (2008) 52-59.

[25] R. Radhakrishnan, A.V. Virkar, S.C. Singhal, "Estimation of charge-transfer resistivity of $La_{0.8}Sr_{0.2}MnO_3$ cathode on $Y_{0.16}Zr_{0.84}O_2$ electrolyte using patterned electrodes", Journal of the Electrochemical Society 152 (1) (2005) 210-218.

[26] H. Iwai, N. Shikazono, T. Matsui, H. Teshima, M. Kishimoto, R. Kishida, D. Hayashi, K. Matsuzaki, D. Kanno, M. Saito, H. Muroyama, K. Eguchi, N. Kasagi, H. Yoshida, "Quantification of Ni-YSZ anode microstructure based on dual beam FIB-SEM technique", 11th International Symposium on Solid Oxide Fuel Cells (SOFC-XI) (2009).

[27] S.V. Patankar, Numerical Heat Transfer and Fluid Flow, Taylor & Francis (1980).

Chapter 3

Novel cell performance enhancement method by mesoscale-structure control in SOFCs

In this chapter, the effect of the mesoscale-structure control on the cell performance is investigated. Because the mesoscale-structure control has a characteristic length of the order close to the effective thickness, a reaction zone would be strongly affected by the mesoscale structure. There is no guarantee that the interface enlargement yields the extension of reaction zone and a resulting enhancement of cell performance. Hence, it is necessary to confirm both experimentally and numerically this enhancement owing to the mesoscale-structure control. Because a numerical simulation can predict the effect of this structure on the distribution of gas concentration, electric potentials and resulting reaction zone, knowledge for the effective mesoscale structure can be obtained numerically. The effect of mesoscale-structure control is investigated on simpler condition. The electrolyte-supported cell and machined mesoscale grooves only on the anode side are adopted due to following reasons. By using the electrolyte-supported cell, we can minimize the effects of the cathode side. The

electrolyte-supported cell is easy to produce and use in power generation experiments in laboratory. The effect of mesoscale-structure control is investigated numerically and discussed the potential and electrochemical reaction distributions, which cannot be measured experimentally. Moreover, the effect of mesoscale-structure control by performing the i-V and impedance measurements is confirmed.

3.1 Methodology

3.1.1 Simulation method

3.1.1.1 Governing equations

In this chapter, the electron, ion and mass transport are considered in the computational model. The electron and ion transport indicate the conservation of the electronic and ionic currents, respectively. Figure 3.1 schematically shows the three layers in the computational domain. The gas diffusion layer covers only the two electrodes and is used to calculate the mass transport inside the porous electrodes. The ionic transport layer covers the entire computational domain and is used to calculate the ionic potential. The electron transport layer covers only the two electrodes and is used to calculate the electronic potential. Figure 3.1 shows the equivalent circuit model in a one-dimensional geometry used to calculate the
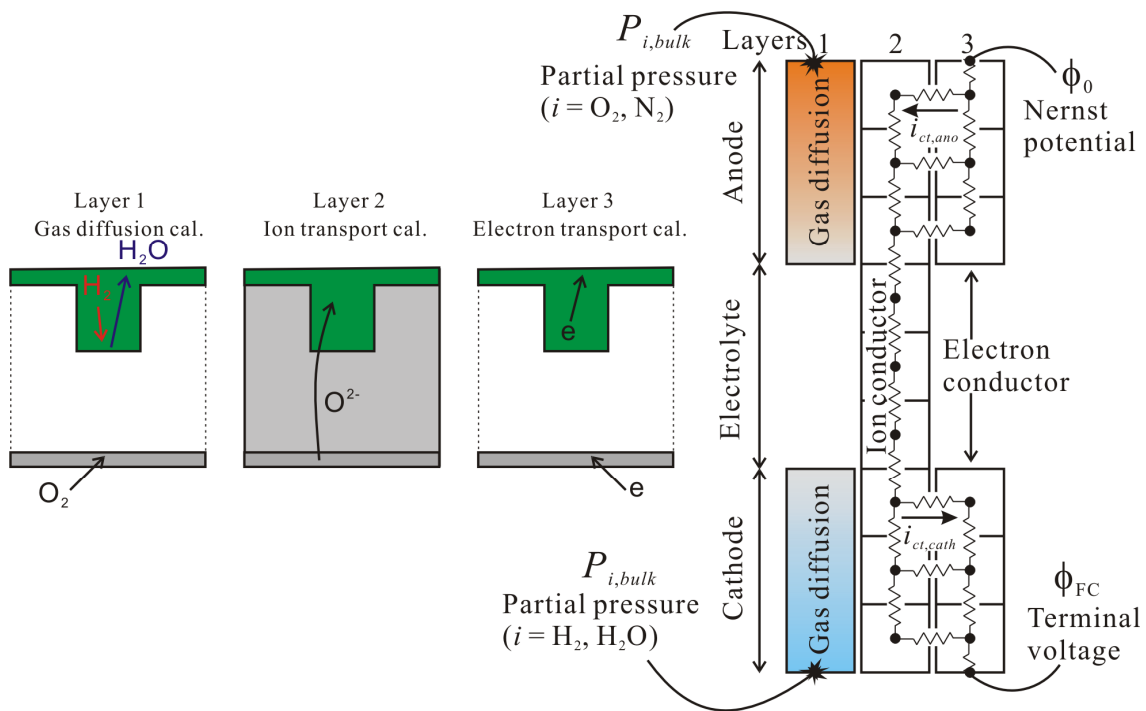

Fig. 3.1 Three layers used for calculation of gas, oxide ion, and electron transport (left) and

electronic and ionic potential fields.

The governing equations for the conservation of electronic and ionic currents are expressed as follows:

$$\frac{\partial}{\partial x}\left(\sigma_{el}^{eff}\frac{\partial \phi_{el}}{\partial x}\right) + \frac{\partial}{\partial y}\left(\sigma_{el}^{eff}\frac{\partial \phi_{el}}{\partial y}\right) = -i_{ct} \tag{3-1}$$

$$\frac{\partial}{\partial x}\left(\sigma_{io}^{eff}\frac{\partial \phi_{io}}{\partial x}\right) + \frac{\partial}{\partial y}\left(\sigma_{io}^{eff}\frac{\partial \phi_{io}}{\partial y}\right) = i_{ct} \tag{3-2}$$

Note that these equations express the conservation of currents at the anode side. When the conservation equations are used at the cathode side, the right-hand sides of these equations take the opposite sign. i_{ct} represents the volume-specific charge transfer current from the electronic phase to the ionic phase.

The dusty-gas model (DGM) is adopted to simulate the mass transport in the anode and cathode. The DGM can be applied when the Knudsen number is nearly equal to unity and is effective for modeling the mass transport in a multicomponent system in a porous medium such as in SOFC electrodes [1-3]. The DGM is written as Eq. (3-3) for each chemical component i of the multicomponent system. The permeability K is estimated from the Carman-Konzeny correlation, given by Eq. (3-4):

$$\frac{N_i}{D_{i,K}^{eff}} + \sum_{j=1,j\neq i}^{n} \frac{X_j N_i - X_i N_j}{D_{ij}^{eff}} = -\frac{P_t}{R_0 T}\nabla X_i - \frac{X_i}{R_0 T}\left(1 + \frac{KP_t}{\mu D_{i,K}^{eff}}\right)\nabla P_t \tag{3-3}$$

$$K = \frac{\epsilon^3}{k_K (1-\epsilon)^2}\left(\frac{V_s}{S}\right)^2 = \frac{\epsilon^3}{k_K (1-\epsilon)^2}\left(\frac{d_{el}}{6}\right)^2 \tag{3-4}$$

For a binary system ($n = 2$), Eq. (3-3) can be separated to find the molar flux of each chemical component, and the conservation equations of each chemical component can be rearranged to Eqs. (3-5)–(3-11):

$$\frac{\partial}{\partial x}\left(\frac{k_1}{R_0 T}\frac{\partial P_1}{\partial x}\right) + \frac{\partial}{\partial y}\left(\frac{k_1}{R_0 T}\frac{\partial P_1}{\partial y}\right) + \frac{\partial}{\partial x}\left(\frac{k_2 P_1}{R_0 T}\frac{\partial P_t}{\partial x}\right) + \frac{\partial}{\partial y}\left(\frac{k_2 P_1}{R_0 T}\frac{\partial P_t}{\partial y}\right) = s_{ct,1} \tag{3-5}$$

$$\frac{\partial}{\partial x}\left(\frac{k_3}{R_0 T}\frac{\partial P_2}{\partial x}\right) + \frac{\partial}{\partial y}\left(\frac{k_3}{R_0 T}\frac{\partial P_2}{\partial y}\right) + \frac{\partial}{\partial x}\left(\frac{k_4 P_2}{R_0 T}\frac{\partial P_t}{\partial x}\right) + \frac{\partial}{\partial y}\left(\frac{k_4 P_2}{R_0 T}\frac{\partial P_t}{\partial y}\right) = s_{ct,2} \tag{3-6}$$

$$s_{ct,\text{H}_2} = \frac{i_{ct}}{2F}, \quad s_{ct,\text{H}_2\text{O}} = -\frac{i_{ct}}{2F} \tag{3-7}$$

$$s_{ct,\text{O}_2} = \frac{i_{ct}}{4F}, \quad s_{ct,\text{N}_2} = 0 \tag{3-8}$$

$$k_1 = \frac{D_{12}^{eff} D_{1,K}^{eff}}{D_{12}^{eff} + D_{m,K}^{eff}}, \quad k_3 = \frac{D_{12}^{eff} D_{2,K}^{eff}}{D_{12}^{eff} + D_{m,K}^{eff}} \tag{3-9}$$

$$k_2 = k_4 = \frac{1}{P_t} \frac{D_{1,K}^{eff} D_{2,K}^{eff}}{D_{12}^{eff} + D_{m,K}^{eff}} + \frac{K}{\mu} \tag{3-10}$$

$$D_{m,K}^{eff} = X_1 D_{2,K}^{eff} + X_2 D_{1,K}^{eff} \tag{3-11}$$

Subscripts 1 and 2 respectively denote H_2 and H_2O on the anode side and O_2 and N_2 on the cathode side. s_{ct} is the molar production or consumption rate of the electrochemical reactions.

The effective diffusivities for binary diffusion and Knudsen diffusion are affected by the properties of the porous electrodes and are expressed as follows:

$$D_{ij}^{eff} = \frac{\epsilon}{\tau} D_{ij} \quad and \quad D_{i,K}^{eff} = \frac{\epsilon}{\tau} D_{i,K} \tag{3-12}$$

$$D_{i,K} = \frac{d_p}{2} \frac{2}{3} \sqrt{\frac{8 R_0 T}{\pi M_i}} \tag{3-13}$$

$$d_p \approx d_h = \frac{4 V_s}{S} \frac{\epsilon}{1 - \epsilon} = \frac{4 d_{el}}{6} \frac{\epsilon}{1 - \epsilon} \tag{3-14}$$

D_{ij} and $D_{i,\text{K}}$ are the binary and Knudsen diffusivity, respectively, and τ is the tortuosity of the porous electrodes.

3.1.1.2 Electrochemical reaction model

In the electrochemical reaction model, the oxidation reaction of hydrogen takes place inside the anode and the reduction reaction of oxygen takes place inside the cathode. The volume-specific charge transfer current of these reactions on the TPB is calculated from the volume-specific length of the TPB, evaluated by the random packing model of binary

spherical particles and empirical correlations of the charge transfer current per unit TPB length based on the experiments with patterned mesh electrodes. The correlations of the charge transfer current per unit TPB length proposed by Nam and Jeon [4] are derived from the experiments of Bieberle et al. [5] for the anode and from those of Radhakrishnan et al. [6] for the cathode, as shown in Eqs. (3-15) and (3-16), respectively. The volume-specific charge transfer current is calculated using Eq. (3-17).

$$i_{tpb,ano}^{L} = \frac{\eta_{act,ano}}{1.645 P_{H_2}^{-0.11} P_{H_2O}^{-0.67} \exp\left(10212/T\right) \times 10^{-4\eta_{act,ano}}} \tag{3-15}$$

$$i_{tpb,cath}^{L} = \frac{R_0 T}{4F} \frac{2\sinh\left(2F\eta_{act,cath}/R_0 T\right)}{0.00136 P_{O_2}^{-0.25} \exp\left(17401/T\right)} \tag{3-16}$$

$$i_{ct} = i_{tpb}^{L} l_{tpb} \tag{3-17}$$

l_{tpb} is the volume-specific length of the TPB in porous electrodes and is referred to as the TPB density.

The activation overpotential in this model is calculated as the potential difference between the electronic and ionic phases in the electrode at each grid, as shown in Eqs. (3-18) and (3-19). This value is used to calculate the charge transfer current.

$$\eta_{act,ano} = \phi_{el} - \phi_{io} - \eta_{con,ano} \tag{3-18}$$

$$\eta_{act,cath} = \phi_{io} - \phi_{el} - \eta_{con,cath} \tag{3-19}$$

The concentration overpotential is calculated as the effect of the partial pressure change on the Nernst potential and is included in the calculations of the activation overpotential.

$$\eta_{con,ano} = \frac{R_0 T}{2F} \ln\left(\frac{P_{H_2,bulk}}{P_{H_2}} \frac{P_{H_2O}}{P_{H_2O,bulk}}\right) \tag{3-20}$$

$$\eta_{con,cath} = \frac{R_0 T}{4F} \ln\left(\frac{P_{O_2,bulk}}{P_{O_2}}\right) \tag{3-21}$$

3.1.1.3 Thermophysical and electrical properties

The effective conductivity is adopted for the porous electrode properties, where we consider the statistical percolation probability. The effective conductivity of an electrode is expressed as follows:

$$\sigma_i^{eff} = (v_i p_i)^{1.5} \, \sigma_i^0 \qquad\qquad (3\text{-}22)$$

In this equation, subscript i denotes an electronic transport phase (el) composed of an electron-conducting material, or an ionic transport phase (io) composed of an ion-conducting material. σ_i^0 is the conductivity (Scm^{-1}) of the dense material i. v_i is the volume fraction of phase i ($v_{el}+v_{io}+\varepsilon=1$). p_i is the percolation probability. The conductivities of the dense materials are given by Eqs. (3-23)–(3-25), and are obtained from the literature [7−9].

$$\sigma_{YSZ}^0 = \left(0.00294 \exp\left(\frac{10350}{T} \right) \right)^{-1} \qquad\qquad (3\text{-}23)$$

$$\sigma_{Ni}^0 = 3.27 \times 10^4 - 10.653T \qquad\qquad (3\text{-}24)$$

$$\sigma_{LSM}^0 = \frac{4.2 \times 10^5}{T} \exp\left(-\frac{1200}{T} \right) \qquad\qquad (3\text{-}25)$$

3.1.1.4 Computational domain

Figure 3.2 shows the computational domains of (a) a standard flat cell and (b) a mesoscale-controlled cell. The mesoscale structure is machined on the anode side of the electrolyte surface to form grooves. The grooves have a rectangular shape and are filled with the anode material as shown in Fig. 3.2(b). The electrolyte, anode and cathode materials are assumed to be YSZ, Ni-YSZ cermet, and LSM-YSZ composite, respectively. We assume isothermal conditions.

We adopt the electrode microscale model proposed by Nam and Jeon [4] and extend it to perform a two-dimensional numerical simulation. This model calculates the electron and ion
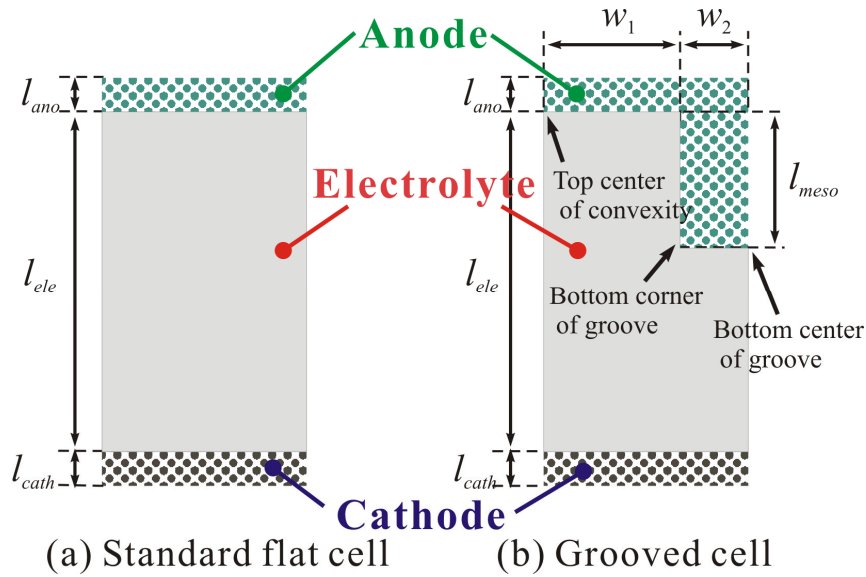
Fig. 3.2 Simulation models of standard flat cell (a) and cell with mesoscale-structure control (b).

3.1.1.5 Calculation conditions

Table 3.1 shows the calculation conditions such as the operating temperature, along with the parameters and properties of the porous electrodes in this simulation. d_{el} and d_{io} are the particle diameters in the electron- and ion-conducting phases, respectively. These values are used to calculate the percolation probability and the TPB density by the random packing model. In the boundary conditions for the gas diffusion layer on the horizontal surface, the partial pressure is given by that of the bulk gas phase from the gas composition at atmospheric pressure. The boundary condition of the electron transport layer is given as the potential difference between the electrode surfaces. In this model, we assume that the electronic potentials of the boundary are given as the Nernst potential, which is calculated using Eq.

Table 3.1 Calculation conditions.

Calculation parameter	Anode	Cathode
Operating temperature T	800 °C	800 °C
Total pressure P_t	0.1013 MPa	0.1013 MPa
Gas compositions	$X_{H_2} : X_{H_2O} = 0.99 : 0.01$	$X_{O_2} : X_{N_2} = 0.21 : 0.7$
Tortuosity factor τ	3.0	3.0
Porosity ϵ	0.3	0.3
Volume fraction of electron-conducting phase v_{el}	0.35	0.35
Volume fraction of ion-conducting phase v_{io}	0.35	0.35
Particle diameter of electron-conducting phase d_{el}	1 μm	1 μm
Particle diameter of ion-conducting phase d_{io}	1 μm1 μm	
Percolation prob. of electron-conducting phase p_{el}	0.925	0.925
Percolation prob. of ion-conducting phase p_{io}	0.925	0.925
TPB density l_{tpb}	1.40 μm^{-2}	1.40 μm^{-2}
Electrode thickness l_i	50 μm	50 μm
Kozeny constant k_K	5	5

Table 3.2 Mesoscale parameters of grooved cell.

	w_1 [μm]	w_2 [μm]	l_{meso} [μm]	l_{ele} [μm]	Mean electrolyte thickness [μm]	Area enlargement factor
Flat cell				433	433	1.00
Case SG	10	5	10	438	433	1.67
Case 1	300	150	200	500	433	1.44
Case 2	200	100	200	500	433	1.67
Case 3	100	50	200	500	433	2.33

(3-26) for the anode surface and using the cell terminal voltage for the cathode surface. We assume that the vertical boundaries of the three layers have symmetric boundary conditions expressed as zero gradients.

$$\phi_0 = E_0 + \frac{RT}{2F} \ln\left(\frac{P_{H_2,bulk}}{P_{H_2O,bulk}} \left(\frac{P_{O_2,bulk}}{10130} \right)^{0.5} \right) \tag{3-26}$$

We focus on the two mesoscale parameters of the anode–electrolyte interface area and the mean electrolyte thickness, because the anode mesoscale structure affects both the anode–electrolyte interface area and the electrolyte thickness. Table 3.2 shows three cases with different values for the mesoscale parameters of the grooved cell. Case SG shows small mesoscale grooves compared with others. Cases 1–3 have the same mean electrolyte thickness but different area enlargement factors, expressed as follows:

50

$$\text{Area enlargement factor} = \frac{\text{Interface area with grooves}}{\text{Interface area without grooves}} = \frac{w_1 + w_2 + l_{meso}}{w_1 + w_2} \qquad (3\text{-}27)$$

The average current density is the total current at the cathode surface boundary divided by the electrode–electrolyte interface area of the flat side, which is expressed as follows:

$$i_{ave} = \frac{\sum\limits_{x} I_{y=0}}{w_1 + w_2} \qquad (3\text{-}28)$$

Note that in this equation, $y = 0$ mm corresponds to the cathode surface.

3.1.2 Experimental method

3.1.2.1 Cell fabrication

Electrode materials are prepared by following the procedure [10]. The cathode material, LSM, is mixed with polyethylene glycol to form a slurry, which is screen-printed on the

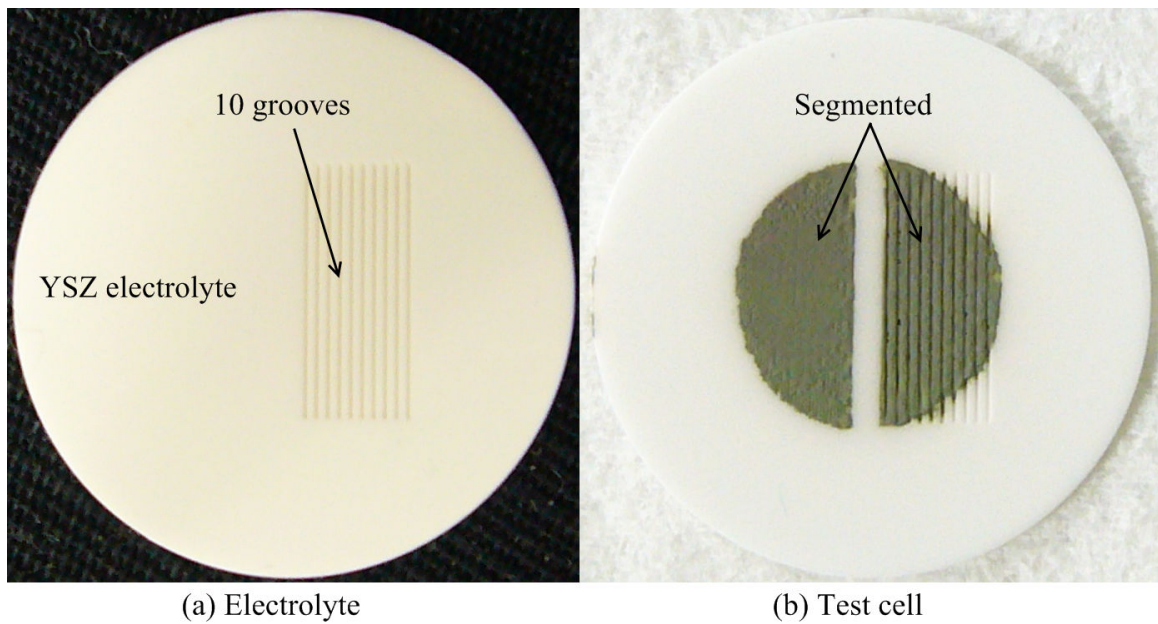(a) Electrolyte   (b) Test cell

Fig. 3.3 Anode-side surface of an electrolyte (a) and a test cell coated with segmented anode (b).

electrolyte and sintered at 1150 °C for 5 h. The anode material, NiO-YSZ, is also mixed with polyethylene glycol, screen-printed on the electrolyte, and sintered at 1400 °C for 5 h. As can be observed in Fig. 3.3(b), the anode electrode is segmented into two parts. The left side of Fig. 3.3(b) shows the flat surface of the electrolyte and the right side shows the grooved surface. Power generation tests using each anode electrode are conducted separately and the results are compared. The reason for using such segmented electrodes rather than preparing two cells (one with a standard flat electrode and the other with a mesoscale structure) is to avoid the issue of the reproducibility of the cells.

Figure 3.3(a) shows the electrolyte of the test cell, which is a small disk-shaped electrolyte made of YSZ with a diameter and thickness of 20 mm and 500 µm, respectively. A surface on the anode side shown in Fig. 3.3(a) is partially machined to realize mesoscale-grooved structures by using the blasting method. The groove width is 200 µm at
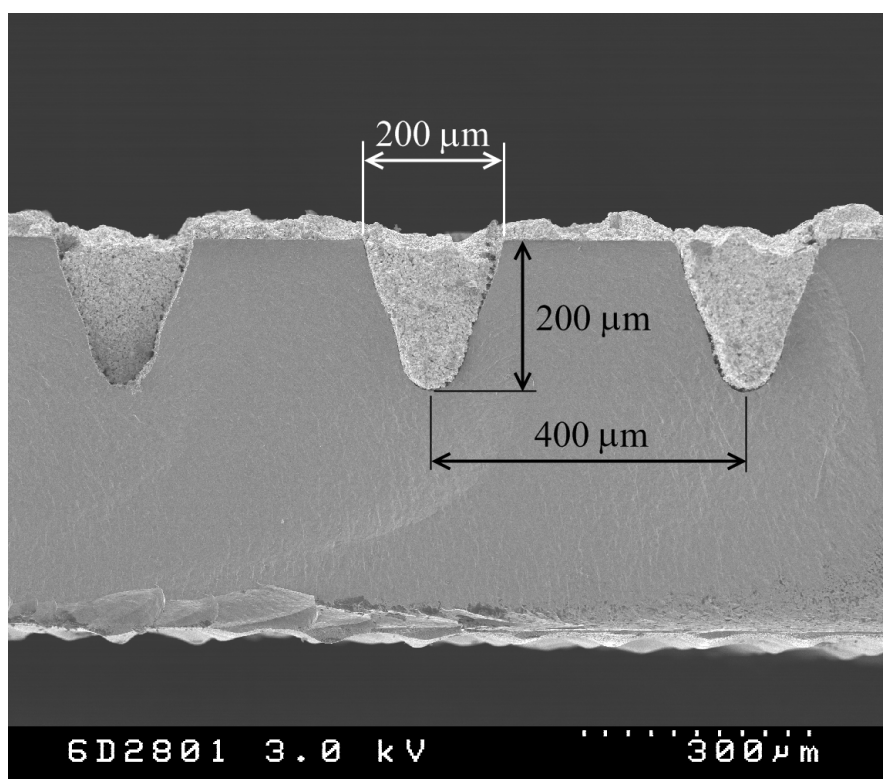

Fig. 3.4 SEM image of part of the grooved area of a cell filled with the Ni-YSZ anode material.

the surface and the distance between two neighboring grooves is 250 μm. The groove shape is not exactly same as the well defined shape in simulation because precise fabrication of rectangular grooves was difficult. Fortunately, uniformity of the groove shape was quite good and therefore we can precisely measure the surface area. The electrolyte surface is flat on the cathode side.

Figure 3.4 is an SEM image showing cross-sectional view of grooved part of a test cell. This image confirms that each groove is 200 μm deep and filled with the anode material. It also confirms that the shape of the grooves is well controlled. The enlargement of the interface area between the electrolyte and anode electrode is estimated to be 60% compared with that for a flat interface. This grooved structure is different to that of the calculation model as indicated above (section 3.2.1).

3.2.2.2 Experimental setup and conditions

In this section, we explain the experimental method used in the power generation test, which involves a segmented electrode with both flat and mesoscale-grooved surface in a button-type cell. The segmented electrode is used to remove the issue of the reproducibility of the cells as much as possible, as it makes it allow the easy comparison of a flat cell with a mesoscale-grooved cell. The power generation performance of each cell is evaluated in terms of the i-V characteristics and impedance spectra.

Figure 3.5 shows a schematic diagram of the experimental apparatus used. A button-type cell is sandwiched between two sets of coaxial ceramic tubes. On the lower side of the anode, fuel is supplied through the inner tube to the cell. It impinges on the cell and then returns through the gap between the inner tube and outer tube to be exhausted. The fuel is a mixture of hydrogen and nitrogen. The hydrogen concentration in the fuel flow is precisely controlled using mass flow controllers. The situation is exactly the same on the upper side of the cathode, but the fluid is dry air. Both outer tubes are tightly connected to the cell by a glass seal to

prevent gas leakage. In the experiments, the hydrogen concentration of the fuel is varied at a constant operating temperature of 800 °C.

In an actual SOFC system, this high operating temperature is self-sustained by heat generated by the electrochemical reactions. However, in a single-cell experiment some additional heat must be supplied to maintain the operating temperature. Therefore, the entire test section is placed in an electric furnace.

To collect the current from the electrodes, a thin platinum mesh is attached to each electrode. As the anode electrode is segmented into two parts, two sets of current collectors are carefully placed on each anode electrode so that there is no electrical contact between the two anode electrodes. A platinum wire with a diameter of 0.5 mm is connected to each platinum mesh and the current is conducted to outside the test section. For voltage measurement, a thinner platinum wire with a diameter of 0.2 mm is also connected to each
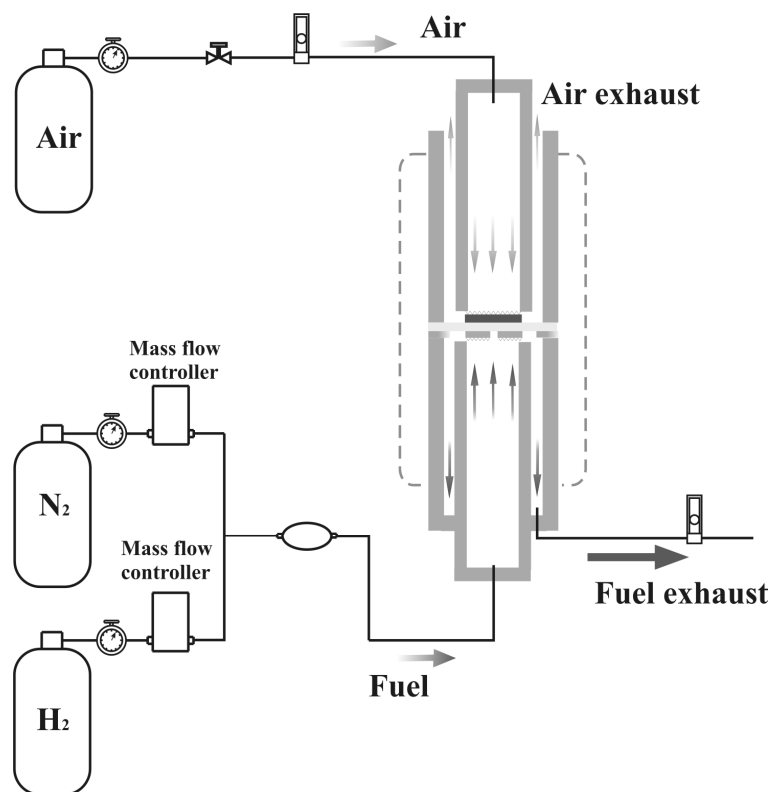

Fig. 3.5 Experimental apparatus used for power generation test involving button-type cell.

platinum mesh. One additional platinum wire is directly connected to the outer part of the electrolyte as a reference electrode. An impedance meter (Kikusui KFM2150) with an electronic load (Kikusui PLZ164WA) is connected to the test cell, as shown in Fig. 3.6, to obtain the i-V curve and perform impedance measurements.
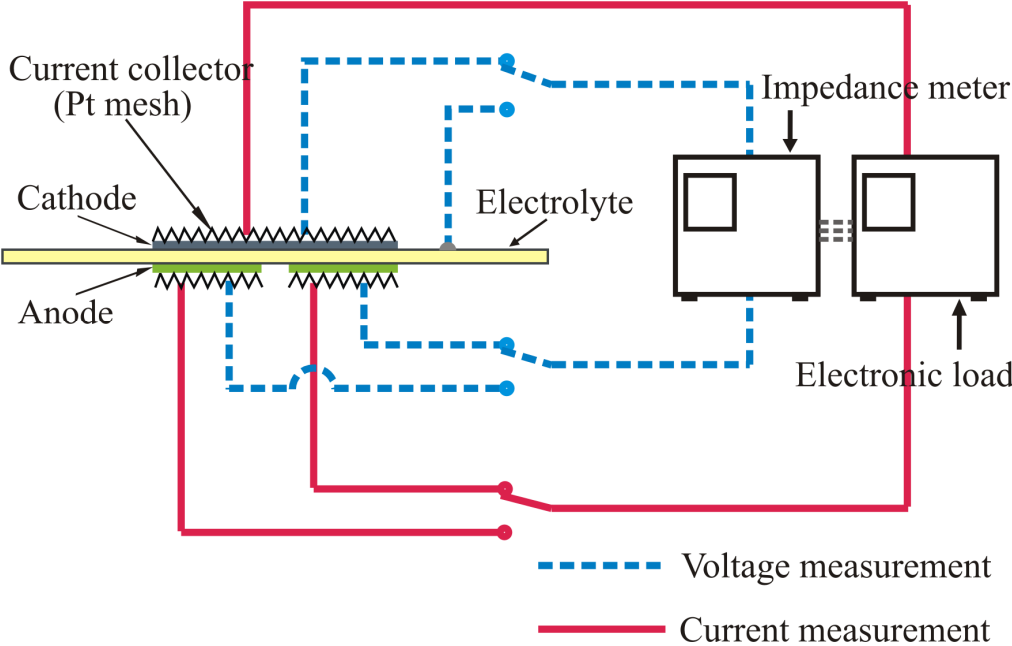

Fig. 3.6 Measurement system used for segmented anode using four-probe method.

3.2 Results and discussion

3.2.1 Simulation results

3.2.1.1 Effect of small anode mesoscale structure

Figure 3.7 shows the distribution of the anode volume-specific charge transfer current at the terminal voltage of 0.5 V in Case SG. This case has the groove height of 10 μm. It is found from this figure that the mesoscale structure is covered with the reaction region when the scale of this structure becomes too small compared with that of the reaction region. The values of average current density of this case and the flat case with the same mean electrolyte thickness are 265 mAcm^{-2} and 259 mAcm^{-2}, respectively. Such structure is not useful to enhance the cell performance. It should be designed that the mesoscale structure becomes larger than the effective thickness of electrode.
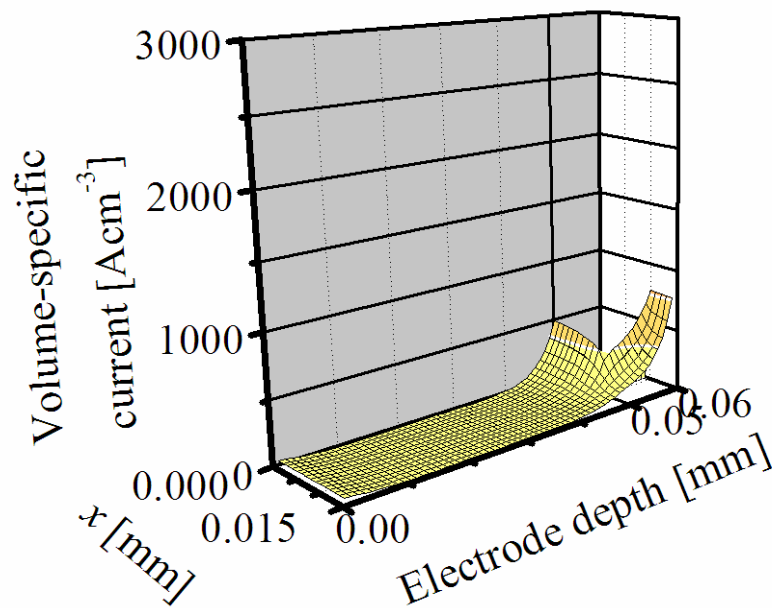

Fig. 3.7 Volume-specific charge transfer current distribution of anode in Case SG.

3.2.1.2 Effect of anode mesoscale structure on i-V characteristics

Figure 3.8 shows the *i-V* characteristics of the cells with grooves (Cases 1–3), along with that of a standard flat cell with an electrolyte thickness of 433 μm.

The characteristics of *i-V* for the mesoscale-grooved cells show a similar trend to that of the flat cell in Fig. 3.8. The terminal voltage decreases almost linearly with increasing current density. The current densities of the grooved cells are almost always larger than that of the flat cell at the same terminal voltage. This confirms that the mesoscale-grooved structure enhances the power generation performance.

Figure 3.9 shows the average current density enhancement, defined as the ratio of the current density of a grooved cell to that of a flat cell having the same electrolyte thickness at the same terminal voltage. This value represents the enhancement of cell performance due to the mesoscale grooves.

$$\text{Average current density enhancement} = \frac{\text{Current density with grooves}}{\text{Current density without grooves}} \tag{3-29}$$

It is shown in Figs. 3.8 and 3.9 that the larger interface area of the grooved cell results in a better cell performance. The average current density enhancement becomes more prominent when the current density is relatively high. The current density enhancement values of Cases 1, 2, and 3 at the terminal voltage of 0.5 V are about 1.08, 1.11, and 1.14, respectively. Because all of the cases in Fig. 11 have the same mean electrolyte thickness, the effect of the mesoscale grooves on the cell performance cannot be ascribed to the mean electrolyte thickness. These enhancement values are less than the area enlargement factor. This is reasonable if we consider the reaction region spread in the electrode as discussed in the previous section. Other reasons can be the thick electrolyte and mal-distribution of current.
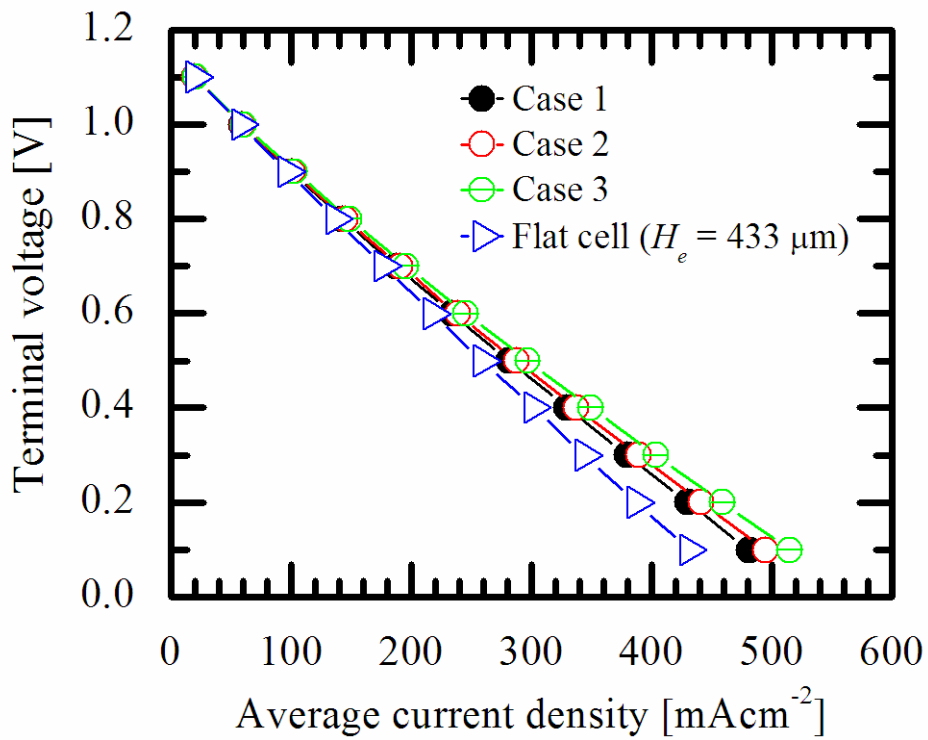
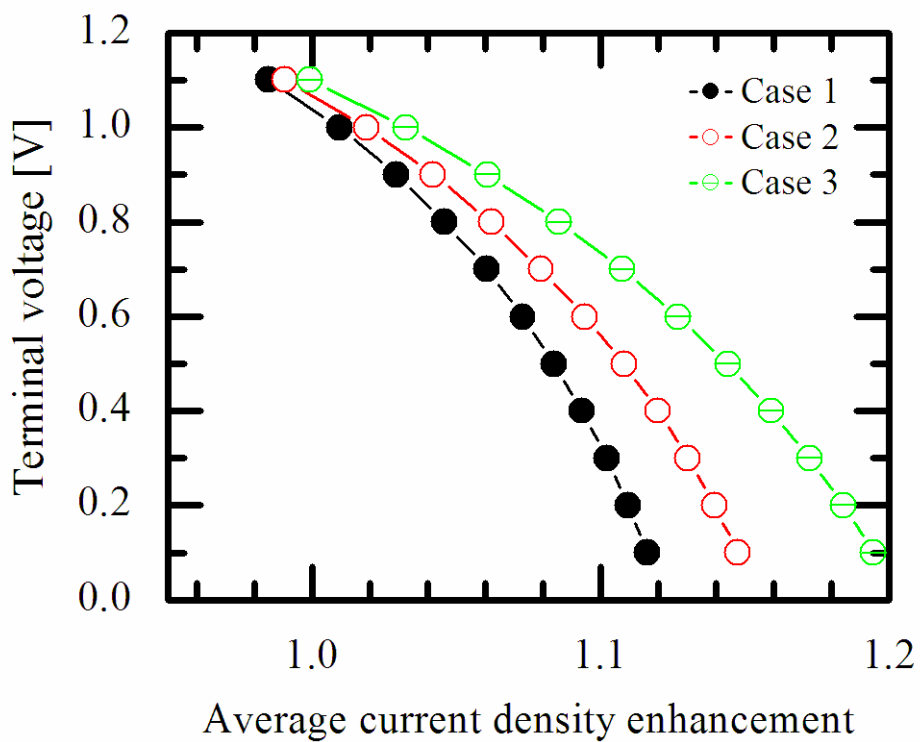Fig. 3.8 *i-V* characteristics of flat cell and grooved cells (Cases 1–3).

Fig. 3.9 Average current density enhancement by mesoscale grooves for Cases 1–3.

3.2.1.3 Electrochemical reaction and electric potential distributions

In this section, we explain in detail the effects of the anode mesoscale grooves from the simulation results for Case 2 at a terminal voltage of 0.5 V. The volume-specific charge transfer current distributions are illustrated in Fig. 3.10 for the flat anode and in Fig. 3.11 for the grooved anode. The volume-specific current corresponds to the local electrochemical reaction rate. Note that in Fig. 3.10, the electrode depths of 0 and 0.05 mm correspond to the anode surface and the flat anode–electrolyte interface, respectively. In Fig. 3.11, the electrode depths of 0, 0.05, and 0.25 mm correspond to the anode surface, the top of a convexity, and groove bottom, respectively.

It can be seen in Fig. 3.10 that the volume-specific current in the flat anode takes a larger value near the anode–electrolyte interface and is distributed uniformly in the x-direction. In the grooved anode, as shown in Fig. 3.11, the volume-specific current is not uniform and is large inside the grooved part, particularly at the bottom corner of groove. This shows that the electrochemical reaction is active at such regions. This region is surrounded by the electrolyte with relatively high ion potential. It leads the ion potential at the bottom corner becomes higher than that of other reaction region. Hence the active electrochemical reaction at such region is reasonable. The sharp edge in the calculation domain may lead an overestimation of the reaction at the bottom corner point.
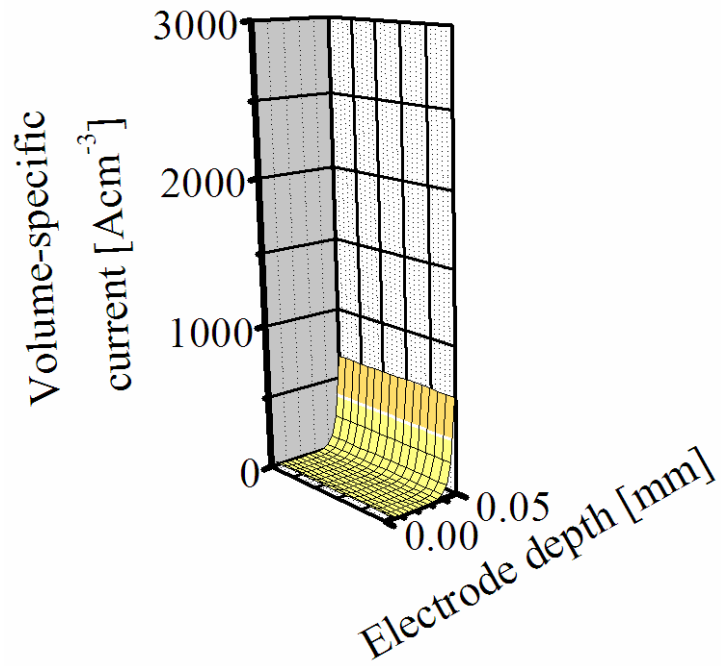
Fig. 3.10 Volume-specific charge transfer current distribution of the flat anode at a terminal voltage of 0.5 V.
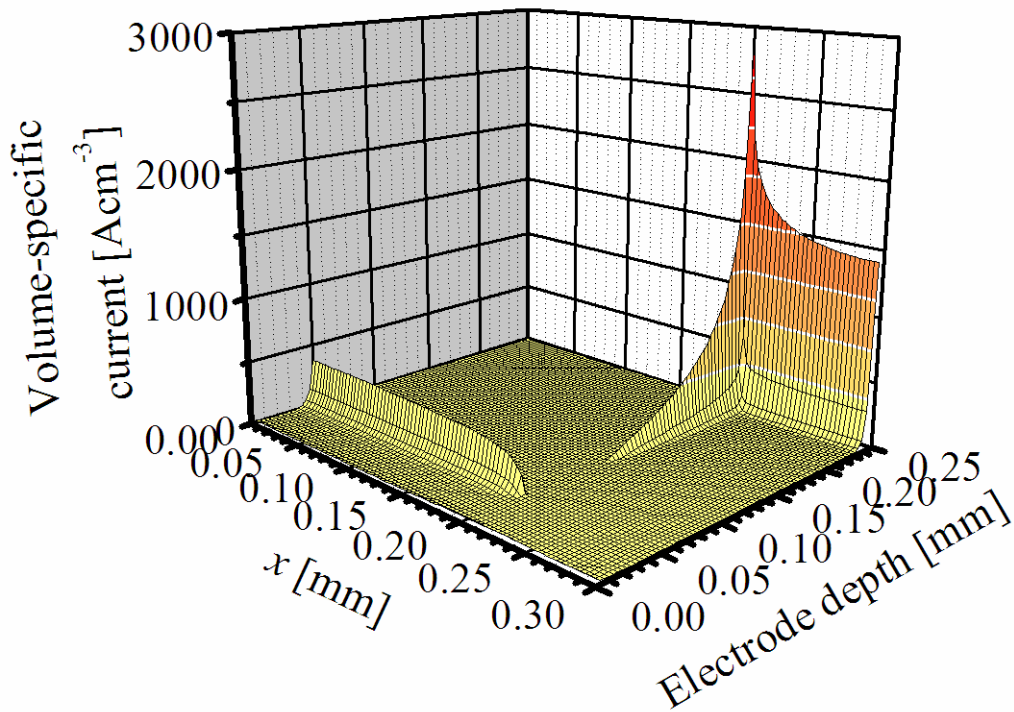

Fig. 3.11 Volume-specific charge transfer current distribution of anode in Case 2 at a terminal voltage of 0.5 V.

This difference in the reaction region is caused by the different electric potentials and different partial pressures of the chemical species. We calculated the electronic and ionic potentials and obtained their distributions in this simulation. The electronic potential field of the electrodes is found to be uniform owing to the low ohmic resistance to electronic conduction of the electrodes. The oxide ion potential fields for Cases 1–3 are illustrated in Fig. 3.12. In this figure, the dashed lines show the electrode–electrolyte interfaces. Note that $y = 0$ mm and $y = 0.6$ mm correspond to the cathode and anode surfaces, respectively. Table 3.3 shows the local values of the activation and concentration overpotentials and the partial
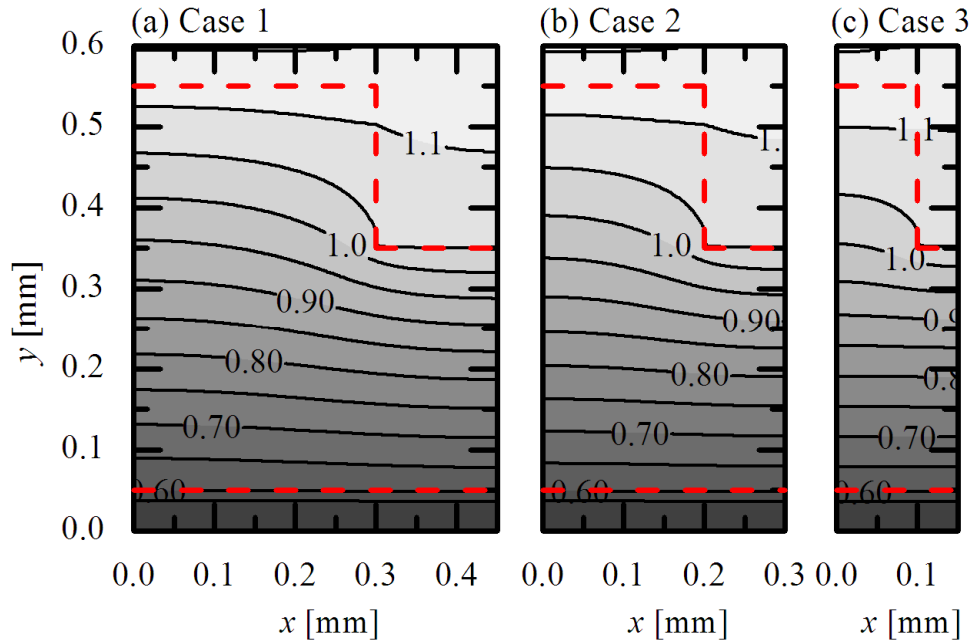

Fig. 3.12 Oxide ion potential fields of (a) Case 1, (b) Case 2, and (c) Case 3 at a terminal voltage of 0.5 V.

Table 3.3 Anode and cathode overpotentials and partial pressures at the top center of convexity, bottom corner of groove, bottom center of groove and cathode bottom at a terminal voltage of 0.5 V in Case 2.

	Location	Depth [μm]	η_{act} [mV]	η_{con} [mV]	P_{H_2} [kPa]	P_{H_2O} [kPa]
Anode	Top center of convexity	50	12	14	1000	1.36
	Bottom corner of groove	250	27	94	952	7.39
	Bottom center of groove	250	15	89	950	6.58
Cathode	Bottom (max)	50	107	0.45		

pressure at some important locations, namely, the top centers of a convexity, the bottom corner of groove, and the bottom center of a groove for the anode, as shown in Fig. 3.2(b), and the cathode–electrolyte interface for the cathode. From Fig. 3.12 and Table 3.3, the large potential difference in the electrolyte shows that the electrolyte resistance is a main resistance due to the thick electrolyte. It can be seen that the potential difference between the anode–electrolyte interfaces at the top of a convexity and the groove bottom is about 0.08 V. Such a potential difference is comparable to the difference between the concentration overpotentials at each location, as shown in Table 3.3, due to the depth of 250 μm. Hence, the activation overpotential of the top of a convexity is comparable to that of the groove bottom. However, the volume-specific current at the groove bottom is at least threefold higher than that at the top of a convexity, because the groove bottom has a relatively high vapor partial pressure, which is affected by the charge transfer current given by Eq. (3-15).

Figure 3.13 shows the proportion of the charge transfer current occurring at the top of a convexity, the side wall of the grooves, and the groove bottom in the three cases. The percentages are calculated from the total charge transfer current up to 10 μm from the
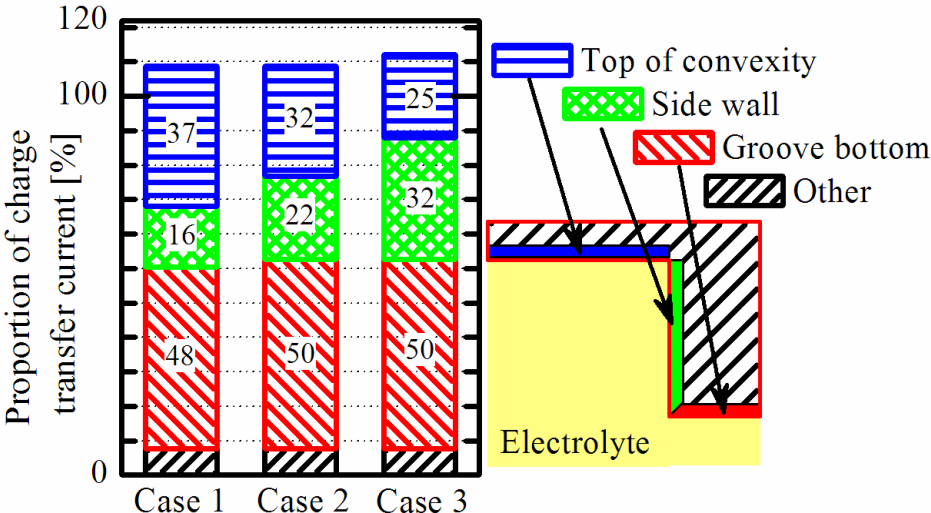

Fig. 3.13 Proportion of charge transfer reaction occurring at the top of a convexity, side wall, and groove bottom in the anode electrode. 100% on the vertical axis indicates the charge transfer current for the flat anode.

electrode–electrolyte interface at the different locations. Note that a value of 100% on the vertical axis represents the total charge transfer current for the flat anode. The percentage of the charge transfer current in the neighborhood of the side wall increases with the area enlargement factor. Hence, this figure indicates that the total charge transfer current increases with the area enlargement factor due to the contribution of the side wall. In these cases, the area enlargement factor is directly related to the proportion of the area corresponding to the side wall, and increases the proportion of the active region because the groove bottom is at a relatively high vapor partial pressure. An increase in the proportion of such an active region yields an increase in the average current density.

3.2.2 Experimental results

In this section, we discuss the effect of the mesoscale-structure control on the power generation performance observed in the experiment. Figure 3.14 shows the i-V curves of the flat and mesoscale-grooved cells. In this figure, the solid triangles and solid circles denote the results for the flat cell and grooved cell, respectively. Note that the flat cell has a different mean electrolyte thickness from the grooved cell. The performance of the grooved cell is higher than that of the flat cell at all terminal voltages. It can be seen that the grooves enhance the cell performance owing to the reduction of the electrolyte thickness and the enlargement of the interface area. The current density of the grooved cell is 25% and 16% higher than that of the flat cell at hydrogen concentrations of 100% and 5%, respectively, at a terminal voltage of 0.5 V.

The experimental current density enhancement does not quantitatively agree with that of simulation. A main reason is the estimation of electrode microstructure by using the random packing model. It is difficult to reconstruct the microstructural parameters of the experimental cell. However, the qualitative agreement of the area enlargement effect between the simulation and experiment is confirmed.

We can clarify the effect of enlarging the electrode–electrolyte interface by considering the impedance spectra measured between the anode and the reference electrode attached to the electrolyte, because the i-V curve includes not only the effect of interface enlargement but also that of decreasing the electrolyte thickness. Figure 3.15 shows a comparison of the impedance spectra of the flat and mesoscale-grooved cells. Impedance arcs related to the anodic electrochemical reaction are observed. Owing to the frequency limit of the measurement system, the left end of each arc is not clear. Because of the grooves, the mean electrolyte thickness is lower for the anode grooves, giving one reason for its better performance. The difference between the ohmic resistances of the two cells is evaluated to be 1.2 Ω using the mean electrolyte thickness. However, from Fig. 17, the difference between the right ends of each arc is about 4.9 Ω (4 Ω at a hydrogen concentration of 5%), which is larger than 1.2 Ω. This means that the thinner electrolyte is not the only reason for the better performance. The concentration overpotential in the anode with grooves is expected to be larger than that for the flat anode. The enhancement of the power generation performance is a result of the apparent decrease in the activation overpotential caused by the enlargement of the active area due to the grooves.
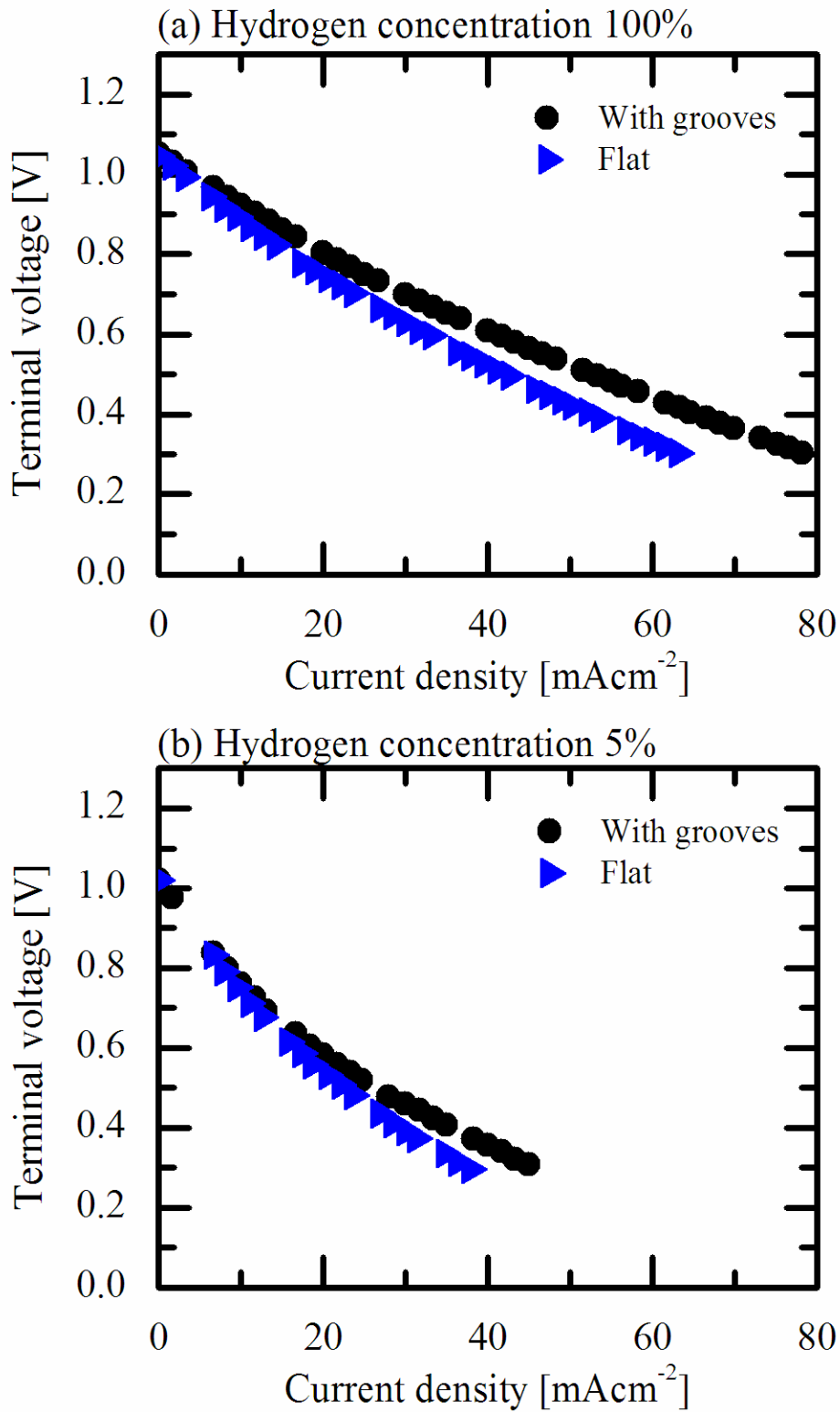
Fig. 3.14 Comparison of *i-V* characteristics of segmented electrodes for cell at operating temperature of 800 °C.
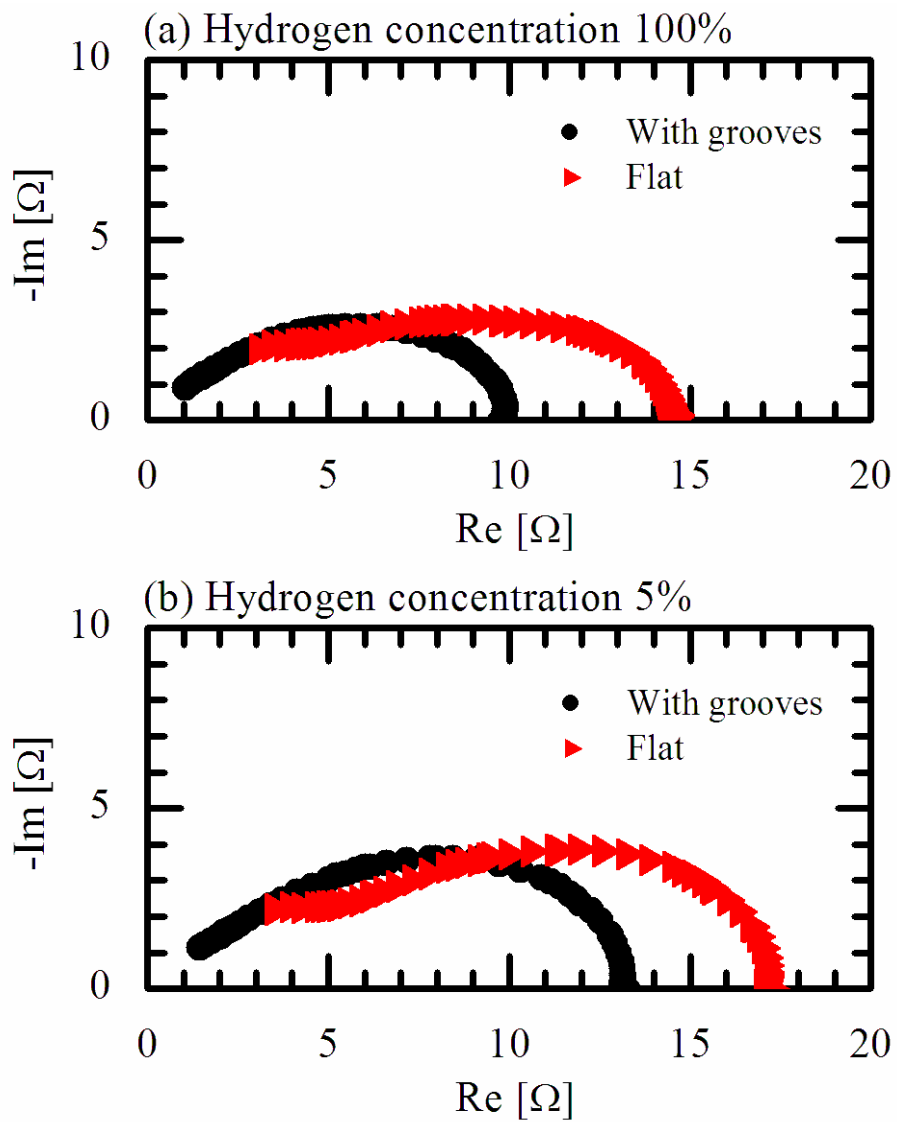
Fig. 3.15 Impedance spectra measured between anode and electrolyte at operating temperature of 800 °C.

3.3 Summary

In this chapter, we numerically and experimentally investigated the effect of mesoscale-structure control on enhancing the power generation performance.

Numerical simulations and power generation experiments were performed to clarify the effectiveness of mesoscale structure. Thick electrolyte was used to focus on one side of the electrolyte, i.e., the anode side, while eliminating the effects of the other side. The microstructural parameters of electrode were estimated on the basis of the random packing model in numerical simulations. The segmented electrode was used in experiments to realize the precise comparison between the flat cell and the mesoscale-grooved cell. We reported the following results.

(1) It was found from the simulation results that the electrochemical reaction is limited to the region close to the electrode–electrolyte interface. The mesoscale-grooved structure was proved to be effective for enhancing the power generation performance, if the groove scale is sufficiently larger than the effective thickness of the electrode.

(2) The qualitative agreement of the area enlargement effect between the simulation and experiment is confirmed. The improvement of the accuracy in the microstructural parameter estimation is required to obtain more quantitative agreement.

(3) From the simulation results of the mesoscale-grooved cell, the electrochemical reaction actively takes place at the groove bottom, because of the similar activation overpotentials and the higher vapor partial pressure compared with those at the top of a convexity.

(4) The expected impedance arc of the grooved cell was smaller than that of the flat cell from the impedance measurement. This confirms that the mesoscale-grooved structure can reduce the reaction resistance.

Reference

[1] E.A. Mason, A.P. Malinauskas, R.B. Evans III, The Journal of Chemical Physics 46 (8) (1967) 3199-3216.

[2] D. Arnost, P. Schneider, The Chemical Engineering Journal 51 (1995) 91-99.

[3] R. Suwanwarangkul, E. Croiset, M.W. Fowler, P.L. Douglas, E. Entchev, M.A. Douglas, Journal of Power Sources 122 (2003) 9-18.

[4] J.H. Nam, D.H. Jeon, Electrochimica Acta 51 (2006) 3446–3460.

[5] A. Bieberle, L.P. Meier, L.J. Gauckler, Journal of the Electrochemical Society 148 (6) (2001) 646-656.

[6] R. Radhakrishnan, A.V. Virkar, S.C. Singhal, Journal of the Electrochemical Society 152 (1) (2005) 210-218.

[7] N.F. Bessette II, W.J. Wepfer, J. Winnick, Journal of the Electrochemical Society 142 (11) (1995) 3792-3800.

[8] U. Anselmi-Tamburini, G. Chiodelli, M. Arimondi, F. Maglia, G. Spinolo, Z.A. Munir, Solid State Ionics 110 (1998) 35-43.

[9] J.R. Ferguson, J.M. Fiard, R. Herbin, Journal of the Power Sources 58 (1996) 109-122.

[10] T. Takeguchi, Y. Kani, T. Yano, R. Kikuchi, K. Eguchi, K. Tsujimoto, Y. Uchida, A. Ueno, K. Omoshiki, M. Aizawa, Journal of Power Sources 112 (2002) 588-595.

Chapter 4

A corrugated mesoscale structure on electrode–electrolyte interface for enhancing cell performance in anode-supported SOFC

In the chapter 3, the electrolyte-supported cells were employed as test cells. However, through a discussion on the relative comparison between reaction resistivity and ion transport resistivity of the electrolyte, it was suggested that surface enlargement by a wavy interface is most effective when the electrolyte is thin. Because a suitable mesoscale structure design as well as its optimization is desired, in this study, we numerically investigate the effect of electrolyte corrugation on the performance of anode-supported cells using a thin electrolyte layer. The effectiveness of this mesoscale-structure control is discussed on the basis of the distributions of electric potential, gas concentration, overpotential and charge transfer current.

4.1 Simulation method

4.1.1 Computational domain and simulation method

Figure 4.1 schematically shows a situation in which the corrugated electrolyte increases the electrode–electrolyte interface area with respect to the apparent electrode area of an anode-supported cell. Here the apparent electrode area denotes the projected area perpendicular to the direction of cell thickness. In this study, however, we address with the case of a rectangular corrugation, for simplicity. By applying the rectangular shape instead of sinusoidal wavy shape, we can clearly separate the electrode into two regions having distinct thicknesses. It is suitable for discussion of gas diffusion.

Figure 4.2 shows the computational domain. A symmetric boundary condition is applied in the x-direction for reducing the computational time. We assume a cell composed of conventional materials, containing a Ni-YSZ cermet anode, a thin YSZ electrolyte and a thin
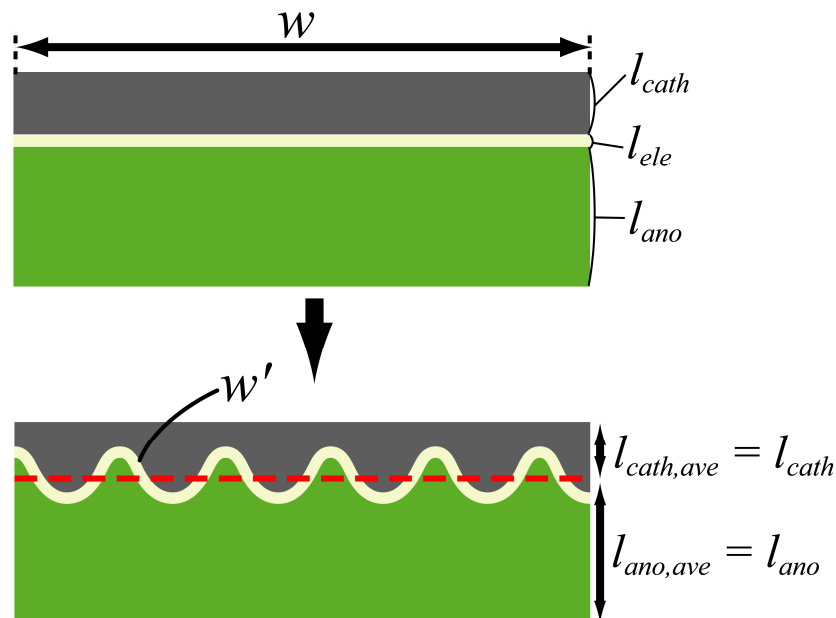

Fig. 4.1 Schematic diagram of corrugated mesoscale-structure control in electrode-supported cell.

70

LSM-YSZ cathode. Because the simulation procedure is the same as that described in the chapter 3, it is only briefly explained here. We performed a steady two-dimensional simulation assuming a constant and uniform temperature of 800 °C. The microstructure of the porous electrodes is modeled by the random packing of spheres [1, 2] with a constant and uniform particle diameter for both ionic and electronic conductors in the electrodes. We consider oxide ion, electron and mass transports in the electrodes, whereas in the electrolyte, we consider only ion transport. The dusty-gas model [3, 4] is used for mass transport in the porous electrodes. This model considers the flow induced by a total pressure gradient and can also be used for the situation in which the effect of Knudsen diffusion is not negligible. The evaluation of the charge transfer current on the TPB is presented in a later section. Combining

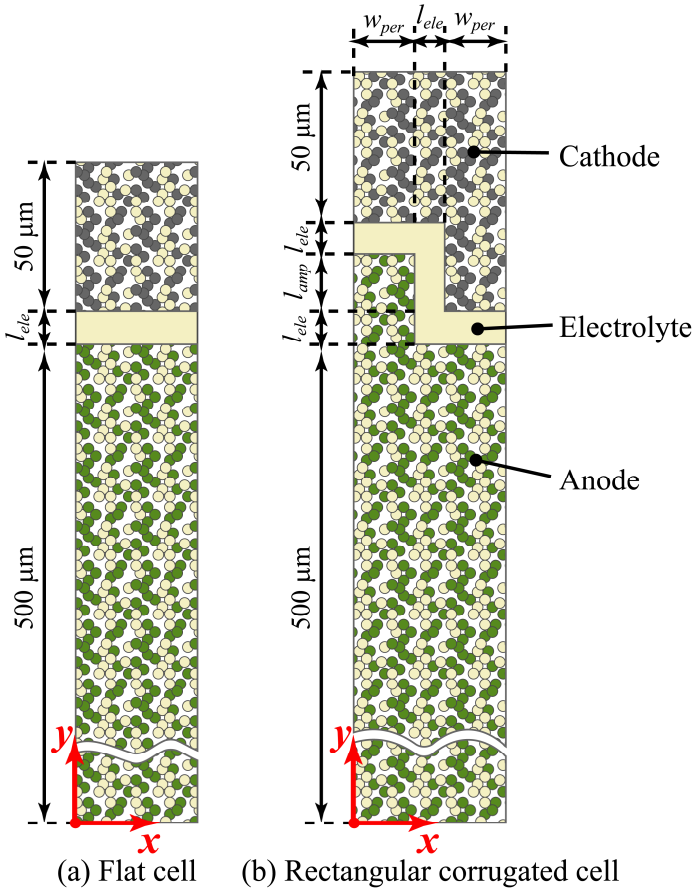(a) Flat cell   (b) Rectangular corrugated cell

Fig. 4.2 Computational model of (a) flat cell and (b) rectangular corrugated cell.

these models, we calculate the distributions of the electric potentials of electron- and ion-conducting phases, the gas concentration and the local electrochemical reaction rate (charge transfer current) [1].

4.1.2 Geometries of cells with electrolyte corrugation

The geometric parameters of the corrugated electrolyte examined in this study are summarized in Table 4.1; their shapes and the lengths, of w_{per} and l_{amp}, are schematically shown in Fig. 4.3. The interface area enlargement factor, α_{area}, is defined simply as follows:

$$\alpha_{area} = \frac{2w_{per} + l_{amp}}{2w_{per} + l_{ele}}$$

(4-1)

To capitalize on the enlargement of the interface, the characteristic length of the corrugation needs to be larger than the effective thickness of the electrode, approximately 10 μm in the chapter 3. Hence, the characteristic length of the corrugation is set at about 50–100 μm in this study. The shortest distances from the electrode surface to the electrode–electrolyte interface are fixed for all electrodes: 50 μm on the cathode side and 500 μm on the anode side (The total thickness of the cell varies with the corrugation amplitude l_{amp}). As a result, it should be noted that a cell with a standard flat interface without corrugation is always in a better condition than the corrugated cells from the view point of concentration overpotential.

Table 4.1 Mesoscale parameters of rectangular corrugated cell.

	w_{per} [μm]	l_{amp} [μm]	l_{ele} [μm]	α_{area}
Case 1	100	40	10	1.14
Case 2	75	40	10	1.19
Case 3	50	40	10	1.27
Case 4	100	90	10	1.38
Case 5	75	90	10	1.50
Case 6	50	90	10	1.73
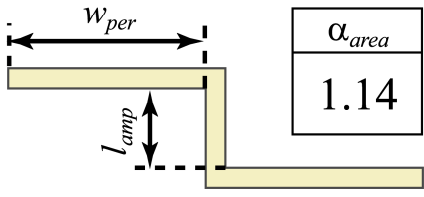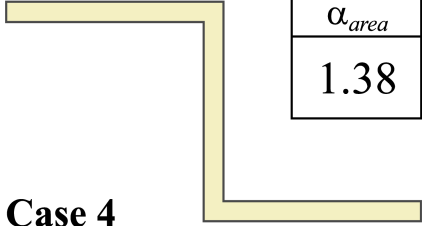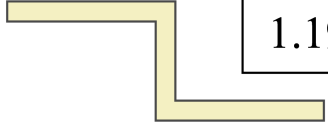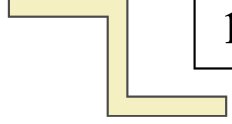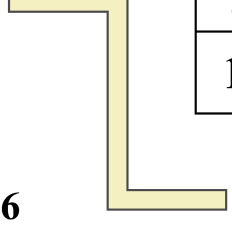
	l_{anp} = 40 μm	l_{amp} = 90 μm
w_{per} = 100 μm	w_{per}, l_{amp}, α_{area} 1.14 **Case 1**	α_{area} 1.38 **Case 4**
w_{per} = 75 μm	α_{area} 1.19 **Case 2**	α_{area} 1.50 **Case 5**
w_{per} = 50 μm	α_{area} 1.27 **Case 3**	α_{area} 1.73 **Case 6**

Fig. 4.3 Six cases with different mesoscale-corrugated electrolytes.

4.1.3 Electrochemical reaction model

In the electrochemical reaction model, the volume-specific charge transfer current on the TPB is calculated from the reaction equation given by Eq. (4-2):

$$i_{ct} = i_0^L l_{tpb} \left[\exp\left(\frac{F}{R_0 T}\eta_{act}\right) - \exp\left(\frac{-F}{R_0 T}\eta_{act}\right) \right] \tag{4-2}$$

where l_{tpb} is the volume-specific length of the TPB in porous electrodes evaluated by the random packing model of spheres, while i_0^L is the exchange current per unit TPB length evaluated by the following empirical equations for the anode [5, 6] and the cathode [7], respectively:

$$i_{0,ano}^{L} = 31.4 P_{H_2}^{-0.03} P_{H_2O}^{0.4} \exp\left(-18300/T\right) \tag{4-3}$$

$$i_{0,cath}^{L} = 1.10 P_{O_2}^{0.5} \exp\left(-16500/T\right) \tag{4-4}$$

4.1.4 Calculation and boundary conditions

Table 4.2 summarizes the calculation conditions. The total pressure and gas composition at the electrode surface are maintained constant. The properties of the porous electrodes are evaluated by the random packing model [1, 2] by assuming uniform particle diameters for the electron- and ion-conducting phases, d_{el} and d_{io}, respectively. The percolation probability and TPB density in Table 4.2 are evaluated on the basis of these assumptions. Figure 4.4 shows the boundary conditions. We apply a symmetric boundary condition in the horizontal (*x*-) direction. The electric potential of the electron-conducting phase at the anode surface is set at the Nernst potential calculated using with Eq. (4-5), while the cell terminal voltage, ϕ_{FC}, applied at the cathode surface is varied in order to change the power generation condition.

$$\phi_0 = E_0 + \frac{RT}{2F} \ln\left(\frac{P_{H_2,bulk}}{P_{H_2O,bulk}} \left(\frac{P_{O_2,bulk}}{10130} \right)^{0.5} \right) \tag{4-5}$$

Table 4.2 Calculation conditions.

Calculation parameter	Anode	Cathode
Operating temperature T	800 ºC	800 ºC
Total pressure P_t	0.1013 MPa	0.1013 MPa
Gas compositions	$X_{H_2} : X_{H_2O} = 0.99 : 0.01$	$X_{O_2} : X_{N_2} = 0.21 : 0.79$
Tortuosity factor τ	3.0	3.0
Porosity ϵ	0.3	0.3
Volume fraction of electron-conducting phase v_{el}	0.35	0.35
Volume fraction of ion-conducting phase v_{io}	0.35	0.35
Particle diameter of electron-conducting phase d_{el}	1 μm	1 μm
Particle diameter of ion-conducting phase d_{io}	1 μm	1 μm
Percolation prob. of electron-conducting phase p_{el}	0.925	0.925
Percolation prob. of ion-conducting phase p_{io}	0.925	0.925
TPB density l_{tpb}	1.40 μm^{-2}	1.40 μm^{-2}

- Cathode surface boundary

$$\phi_{el} = \phi_{FC}$$

$$\frac{\partial \phi_{io}}{\partial y} = 0$$

$$P_{O_2} = P_{O_2,bulk} \qquad P_{N_2} = P_{N_2,bulk}$$

- Symmetric boundary

$$\frac{\partial \phi_{el}}{\partial x} = 0$$

$$\frac{\partial \phi_{io}}{\partial x} = 0$$

$$\frac{\partial P_i}{\partial x} = 0$$

$$(i = H_2, H_2O, O_2, N_2)$$

- Anode surface boundary

$$\phi_{el} = \phi_0$$

$$\frac{\partial \phi_{io}}{\partial y} = 0$$

$$P_{H_2} = P_{H_2,bulk}$$

$$P_{H_2O} = P_{H_2O,bulk}$$

Cathode

Electrolyte

Anode

$\phi_0 - \phi_{FC} = \eta_{cell}$
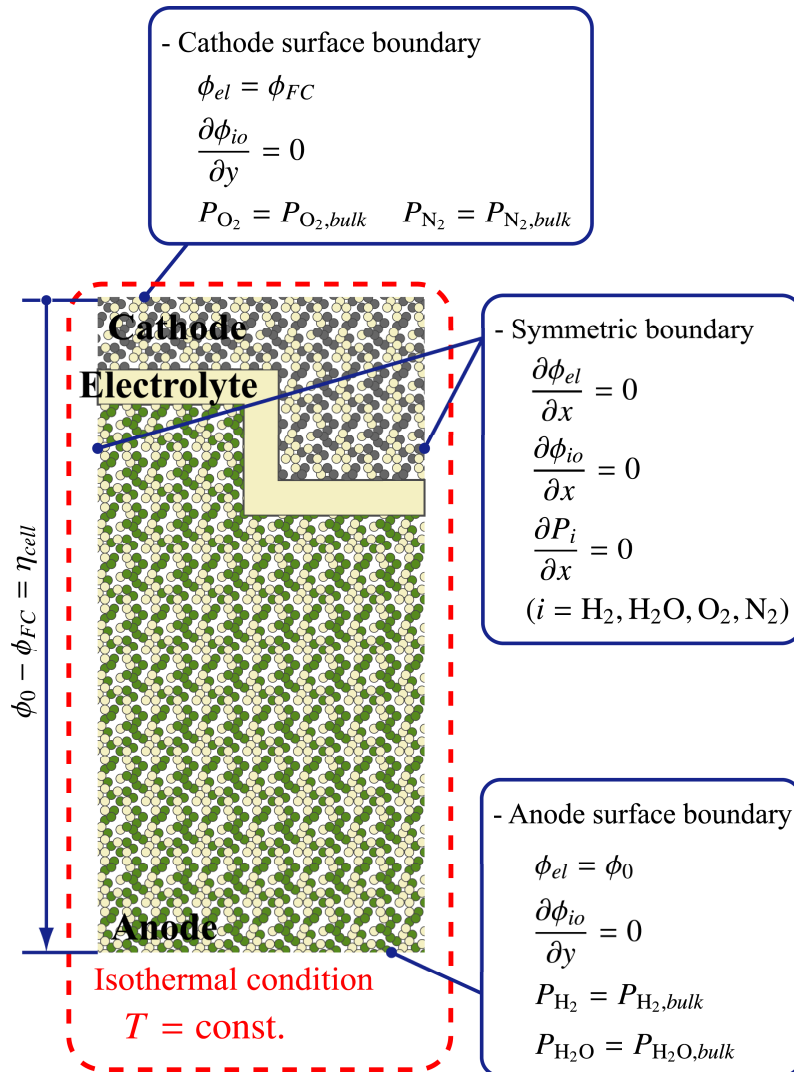
Isothermal condition
T = const.

Fig. 4.4 Calculation and boundary conditions.

4.1.5 Evaluation of losses

The ohmic, activation and concentration losses measured in the experiments are regarded as macroscopic values based on the local distributions. Therefore, for such a conventional discussion of cell performance, it is useful to evaluate the representing mean values for each loss on the basis of the simulation results, as follows.

Activation and concentration losses

We can write the mean values as Eqs. (4-6) and (4-7).

$$\eta_{act,ano}^{m} = \frac{\int \eta_{act,ano} i_{ct} dV}{I_t} \;, \quad \eta_{act,cath}^{m} = \frac{\int \eta_{act,cath} i_{ct} dV}{I_t} \tag{4-6}$$

$$\eta_{con,ano}^{m} = \frac{\int \eta_{con,ano} i_{ct} dV}{I_t} \;, \quad \eta_{con,cath}^{m} = \frac{\int \eta_{con,cath} i_{ct} dV}{I_t} \tag{4-7}$$

where I_t and i_{ct} are the total current and the local charge transfer current, respectively, and V is the volume of the computational domain.

Ohmic loss

We define the local ohmic loss as the potential difference between an arbitrary point in the electrode and a reference potential. It can be calculated if a definite reference potential can be specified at the reference point. Because the electric potential of the electron-conducting phase at the electrode surface is uniform and constant in this study, we set the reference point at the electrode surface for the electron transport. We calculate the representing mean ohmic loss associated with electron transport as

$$\eta_{ohm,el,ano}^{m} = \frac{\int (\phi_0 - \phi_{el}) i_{ct} dV}{I_t} \;, \quad \eta_{ohm,el,cath}^{m} = \frac{\int (\phi_{el} - \phi_{FC}) i_{ct} dV}{I_t}. \tag{4-8}$$

For the case of ion transport, it is possible to set the reference point at the electrode–electrolyte interface if the cell is flat. In this case, we can write the mean ohmic loss associated with ion transport in the electrode as

$$\eta^m_{ohm,io,ano} = \frac{\int (\phi_{io} - \phi_{int,ano}) i_{ct} dV}{I_t} \ , \quad \eta^m_{ohm,io,cath} = \frac{\int (\phi_{int,cath} - \phi_{io}) i_{ct} dV}{I_t}. \tag{4-9}$$

However, when the interface has a mesoscale structure, a definite reference potential cannot be specified anywhere in the electrodes. Hence, for the case of corrugated cells, we calculate the representing mean ohmic loss associated with ion transport as the difference between the total loss of the cell and the sum of the losses expressed by Eqs. (4-6)−(4-8):

$$\begin{aligned}
\eta^m_{ohm,io} &= \eta_{cell} - \sum_i \eta^m_i \\
&= \phi_0 - \phi_{FC} - \eta^m_{act,ano} - \eta^m_{con,ano} - \eta^m_{ohm,el,ano} - \eta^m_{act,cath} - \eta^m_{con,cath} - \eta^m_{ohm,el,cath}
\end{aligned} \tag{4-10}$$

4.2 Results and discussion

4.2.1 Effect of corrugated structure on distributions of reaction field

First, we discuss the fundamental influences of the corrugated structure on distributions, such as the gas partial pressure, the electric potentials of electron- and ion-conducting phases, the activation overpotential, the concentration overpotential and the volume-specific charge transfer current. We focus our discussion on the results of Case 4, with an average current density of 1000 mAcm^{-2}; average current density is defined as the value of the total current divided by the apparent electrode area.

Figure 4.5 shows partial and total pressure distributions: (a) partial pressure of oxygen for the cathode and of hydrogen for the anode; (b) partial pressure of nitrogen for the cathode and of water vapor for the anode; (c) total pressure fields in the cathode and anode. Note that the value of the color contour differs in each distribution. Because oxygen and hydrogen diffusing from the electrode surfaces are consumed in the vicinity of the cathode– and anode–electrolyte interfaces, respectively, these partial pressures decrease with increasing electrode depths. On the other hand, the partial pressure of water vapor produced on the anode-side increases with the electrode depth. In addition, the partial pressure of nitrogen on the cathode-side increased with the electrode depth because nitrogen is driven to the interface by a total pressure gradient caused by oxygen consumption in the vicinity of the interface. In addition to the above-mentioned features, primarily in the vertical direction of the figures, we can distinctly observe the effects of the corrugated structure on the pressure difference along the electrode–electrolyte interface.

Figure 4.6(a) and (b) show the electric potential distributions of electron- and ion-conducting phases, respectively. The electric potential of the electron-conducting phase shown in Fig. 4.6(a) is almost uniform in both electrodes because of high electronic conductivities; this implies that the effect of electronic conduction on the cell performance in
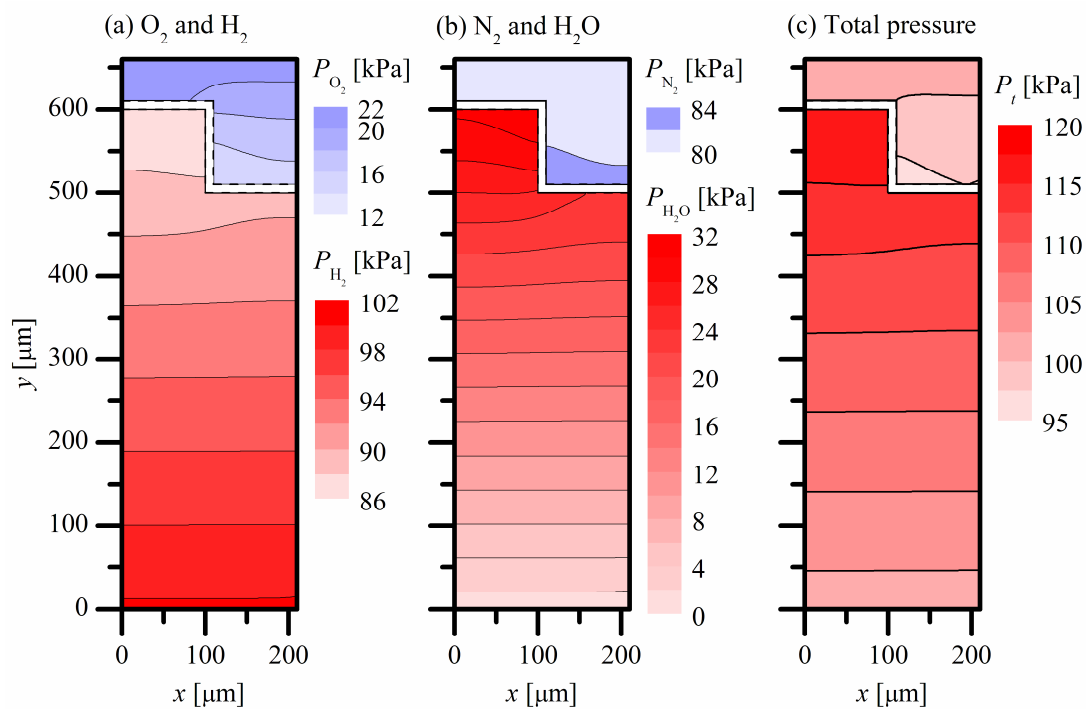
Fig. 4.5 Pressure distributions of (a) O_2–H_2 partial pressure, (b) N_2–H_2O partial pressure and (c) total pressure, for Case 4.
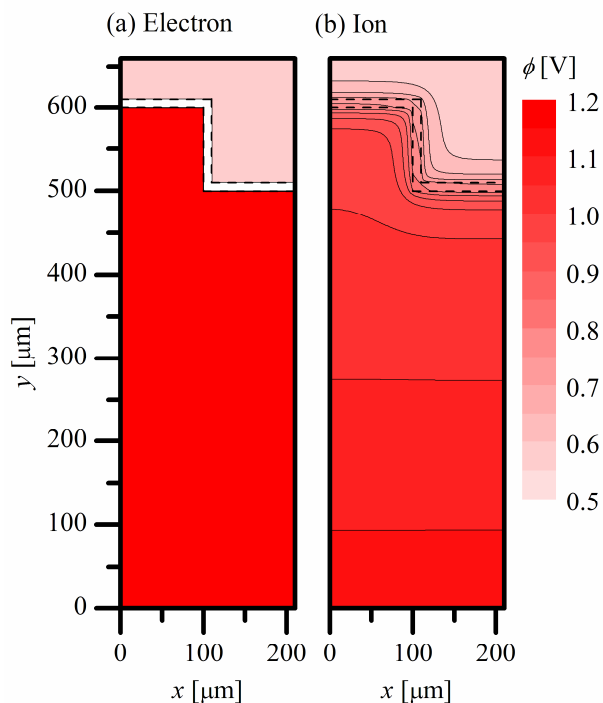

Fig. 4.6 Electric potential distributions of (a) electron- and (b) ion-conducting phases for Case 4.

the electrodes is negligible. On the other hand, the electric potential of the ion-conducting phase shown in Fig. 4.6(b) significantly changes around the electrolyte because the charge transfer reaction occurs in the vicinity of the electrode–electrolyte interface. The ohmic loss is caused by the ionic current that flows through the electrolyte from the cathode to the anode.

Figure 4.7(a) shows the distribution of the activation overpotential evaluated from the electric potentials and the concentration overpotential. It can be determined from this figure that the trend of the activation overpotential almost corresponds to that of the electric potential of the ion-conducting phase. Figure 4.7(b) shows the distribution of the concentration overpotential. Because concentration overpotential depends on partial pressure, it increases in the regions of diluted oxygen for the cathode and of diluted hydrogen and concentrated water vapor for the anode. The concentration overpotential is negligibly small on the cathode side and had a maximum value of approximately 0.16 V on the anode side. The variation of the concentration overpotential along the anode–electrolyte interface was found to be less than 0.02 V. Hence, it is observed that the differences in the concentration
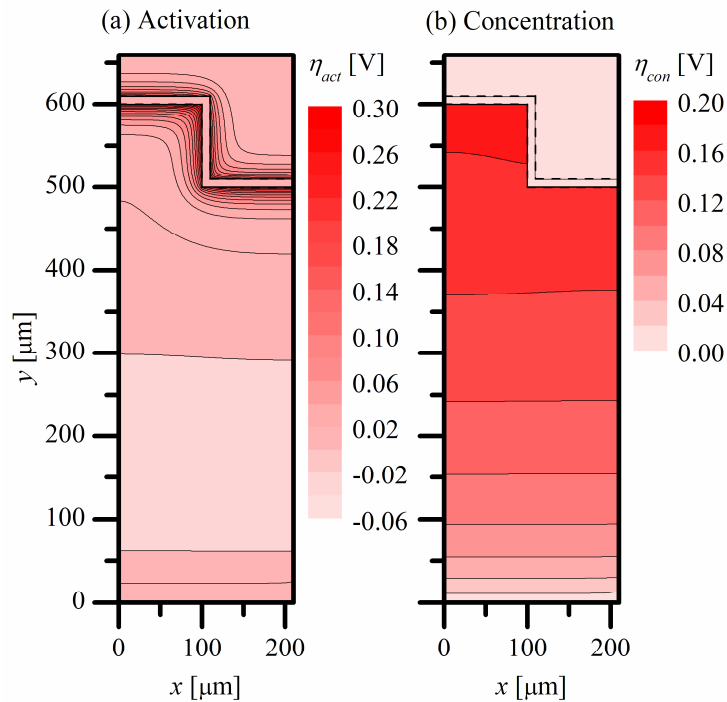

Fig. 4.7 Overpotential distributions of (a) activation and (b) concentration, for Case 4.

overpotential in the reaction zone of each electrode are relatively small.

Figure 4.8 shows the distribution of the volume-specific charge transfer current focused around the electrolyte. The charge transfer current takes high values in the region near the electrolyte. We define an active reaction zone as the zone where the volume-specific charge transfer current is more than 10 % of its maximum value. In this figure, the dashed-red lines show the outer limit of the active reaction zones on both anode and cathode sides. It can be observed from Fig. 4.8 that the thickness of the active reaction zone is approximately 20 μm on anode side and 10 μm on cathode side. This figure indicates that the trend of the charge transfer current agrees with those of the activation overpotential and electric potential of the ion-conducting phase. From this result, the active reaction zone is found to strongly depend on the electric potential of the ion-conducting phase. For comparison, the distribution of the volume-specific charge transfer current at the same current density as for Case 1 is illustrated in Fig. 4.9. The active reaction zone is also marked in this figure. The active reaction zones for Case 1 also distributes in the electrodes within 20 μm for anode and 10 μm for cathode from each electrode interfaces. In Case 1, the variation of the concentration overpotential along the anode–electrolyte interface was even smaller than Case 4 and was less than 0.01V. Although slight difference is observed in the variation of the concentration overpotential along the interfaces between Cases 1 and 4, its effect on the active reaction zone is limited. There is no appreciable difference in the active reaction zone between Cases 1 and 4. Hence, the positive effect of increasing the amplitude of the corrugated structure is superior to the negative effect associated with increasing the concentration overpotential. As intended, this effective thickness of the reaction zone was determined to be much smaller than the scale of the corrugated structure. Thus, the enlargement of the reaction zone by the corrugated structure results in a reduction in the local charge transfer and ionic current, thereby reaching the overpotential reductions and consequently enhancing cell performance.
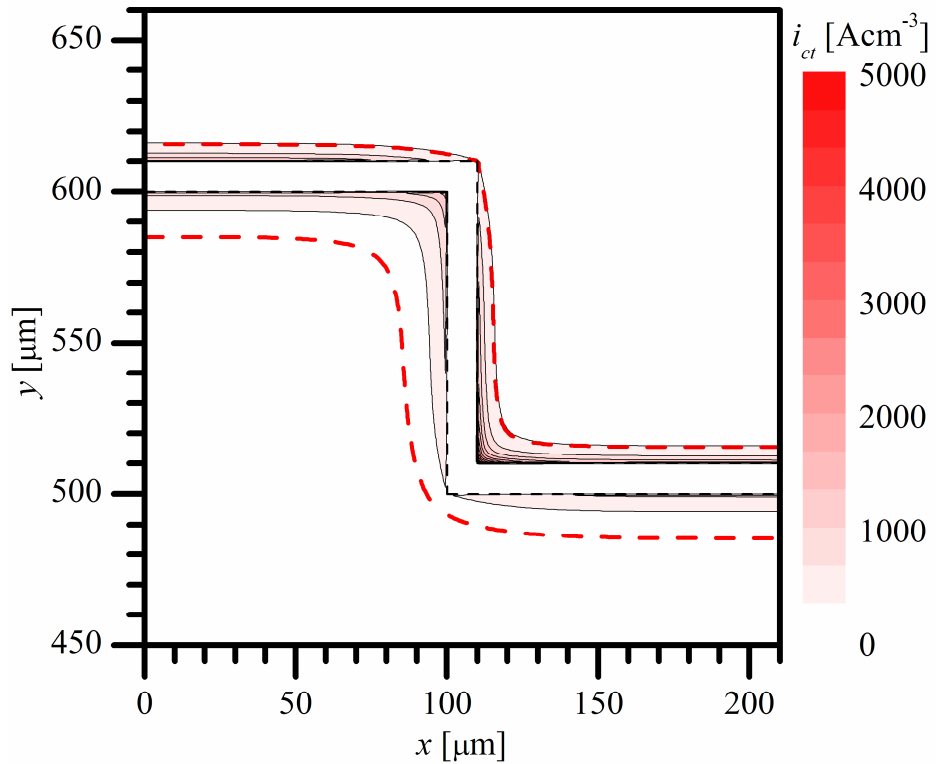
Fig. 4.8 Volume-specific charge transfer current distribution with active reaction zone around electrolyte for Case 4.
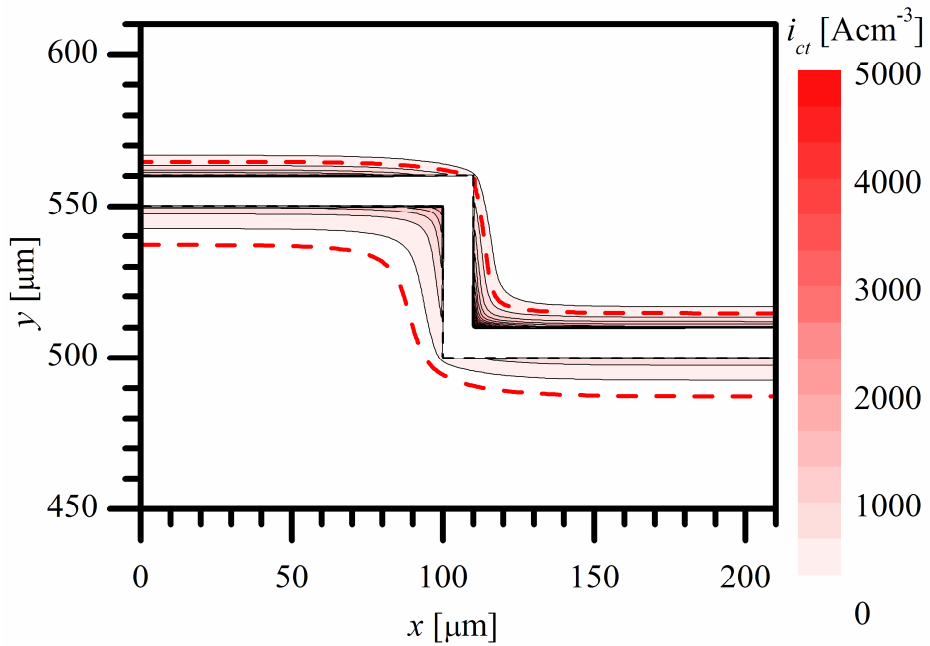
Fig. 4.9 Volume-specific charge transfer current distribution with active reaction zone around electrolyte for Case 1.

4.2.2 Overall cell performance

Figure 4.10 shows the *i-V* and *i-P* characteristics for Case 4 together with the results for a flat cell. It is observed that the mesoscale-corrugated cell enhanced the power generation performance compared to the flat cell. The maximum power density for Case 4 is 32 % higher than that for the flat cell. This improvement is achieved because the positive effect, primarily caused by the interface enlargement, is more prominent than the negative effects associated with the increased concentration overpotential and the ohmic loss.

Figure 4.11 shows the average current density enhancement, defined as the ratio of the average current density of a corrugated cell to that of a flat cell at the same terminal voltage, as follows:

$$\text{Average current density enhancement} = \frac{\text{Average current density of corrugated cell}}{\text{Average current density of flat cell}} \quad (4\text{-}11)$$

Solid symbols indicate cases with shallow corrugation (Cases 1–3), whereas solid-white
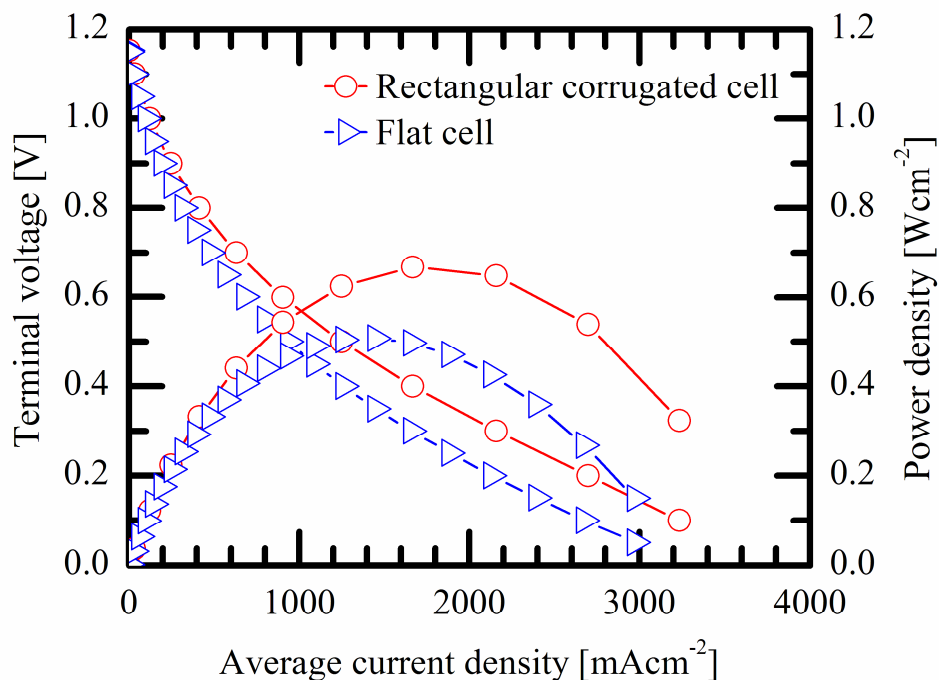
Fig. 4.10 Characteristics of *i-V* and *i-P* for Case 4.

symbols indicate cases with deep corrugation (Cases 4–6). The figure shows that, in all cases, the average current density enhancement takes a value larger than unity. The degree of enhancement is closely related to the interface area enlargement factor of the corrugated cell. A cell with a larger interface enlargement factor results in a larger average current density enhancement. Case 6 achieves an enhancement of 63 % at a terminal voltage of 0.6 V. It is also noted that there exists a maximum value of the average current density enhancement for each case. That is, starting from the higher terminal voltage, the average current density enhancement increases as the terminal voltage decreases. The decrease at the relatively low terminal voltage range is ascribed to the increase of the concentration overpotential due to the relatively high current density, and its effect is more prominent in the cases with deep corrugation (Cases 4–6). The maximum value is obtained at relatively high terminal voltage for the deep-corrugation cases because the effect of the concentration overpotential increases with the increasing depth of the electrode. Hence, the effect of the concentration overpotential cannot be neglected for the deep-corrugation case and for the relatively high average current density condition.

Fig. 4.11 Average current density enhancement by corrugated electrolyte.

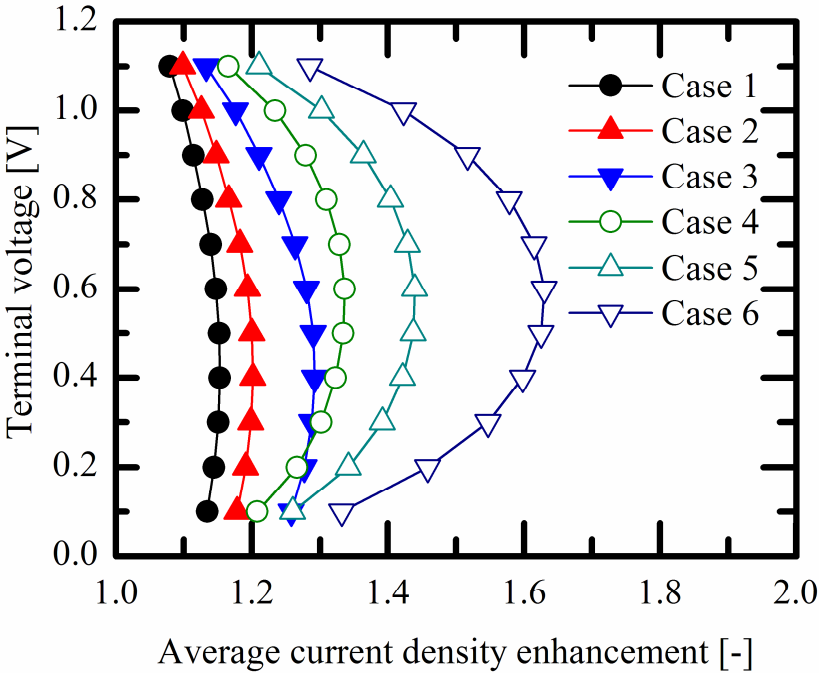Table 4.3 summarizes the mean losses of the cells calculated at an average current density of 1000 mAcm^{-2}. The three mean ohmic losses by ion transport in each component (cathode, anode and electrolyte) are shown separately in the flat cell, while the total value of the mean ohmic loss by ion transport is shown for the corrugated cells because the mean ohmic loss of the corrugated cell cannot be separated into cell components as explained in section 4.1.5. The mean ohmic loss by electron transport and the mean cathode concentration overpotential are negligibly small compared to the total loss. The mean anode concentration overpotential is relatively large but is not affected by the corrugated shape under the conditions indicated in of Table 4.3. The total ohmic loss by ion transport and the mean activation overpotential in the mesoscale-corrugated cells considerably decrease with increase in the interface area enlargement factor. This confirms the positive effect of the reduced local current by the interface area enlargement. Table 4.4 shows the maximum power density of the cells. The maximum power density is increased by the interface area enlargement factor and is enhanced by 59% for Case 6.

Table 4.3 Total and mean overpotentials at average current density of 1000 mA/cm^2.

			Flat	Case 1	Case 2	Case 3	Case 4	Case 5	Case 6
	Total	[mV]	674	629	617	595	583	560	525
	Reduction	[%]		6.6	8.5	11.7	13.5	16.8	22.1
Cathode	Ohm (electron)	[mV]	0.02	0.03	0.03	0.03	0.05	0.05	0.05
	Ohm (ion)	[mV]	73						
	Activation	[mV]	118	111	109	105	101	96	89
	Concentration	[mV]	1.68	3.22	3.33	3.52	5.19	5.43	5.82
Anode	Ohm (electron)	[mV]	0.01	0.01	0.01	0.01	0.01	0.01	0.01
	Ohm (ion)	[mV]	121						
	Activation	[mV]	161	147	144	137	127	120	109
	Concentration	[mV]	153	154	154	155	157	158	158
Electrolyte	Ohm (ion)	[mV]	45						
Total	Ohm (ion)	[mV]	240	213	206	194	192	181	163

Table 4.4 Maximum power density and its enhancement for certain cases.

		Flat	Case 1	Case 2	Case 3	Case 4	Case 5	Case 6
Max. power density	[mW/cm^2]	507	581	606	652	667	717	806
Enhamcement	[%]		15	19	28	32	41	59

4.2.3 Effect of porosity

It is shown in the previous discussion with the help of Fig. 4.11 that the degree of performance enhancement can be suppressed by the concentration overpotential even though the porosity in the porous electrodes is assumed to be reasonably high in the above calculations. Hence we examine the effect of the anode porosity reduced from its original value of 0.3 to 0.1. We focus on the anode side not only because we assume an anode-supported cell in this study but also because its porosity may change during a long-term operation. The microstructure may change for various reasons such as thermal cycle, redox cycle and carbon deposition.

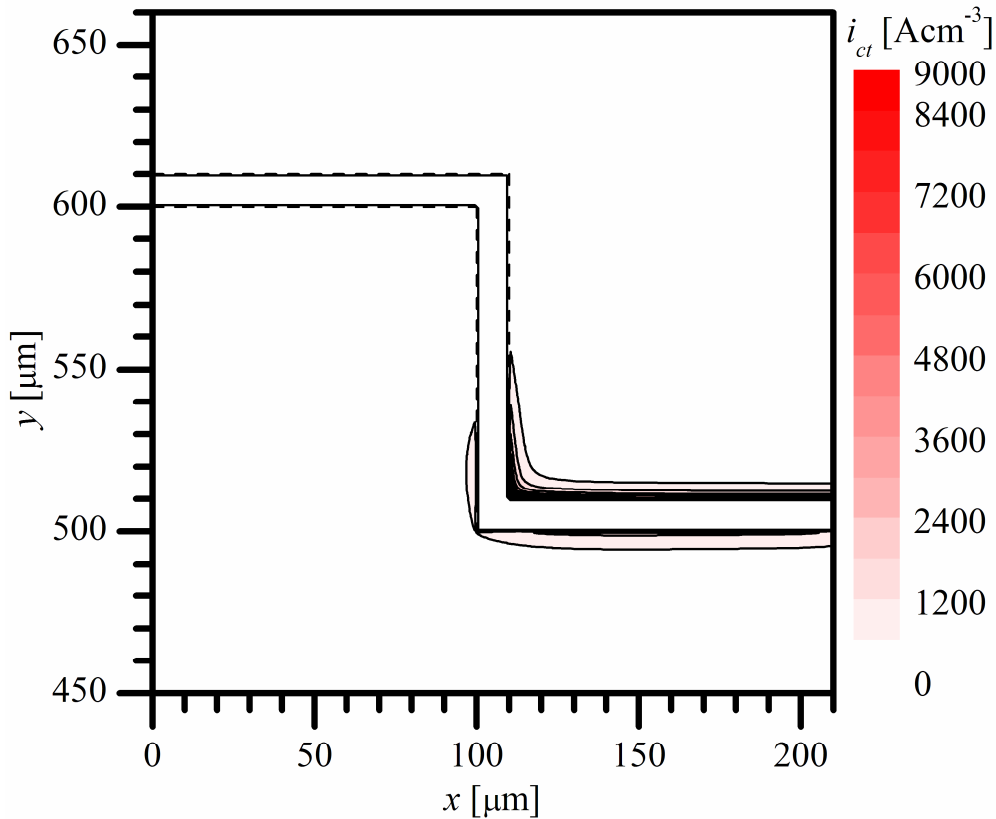Figure 4.12 shows the distribution of the volume-specific charge transfer current for a

Fig. 4.12 Volume-specific charge transfer current distributions for Case 4 at average current density of 1000 mAcm^{-2} under low anode porosity condition ($\varepsilon_{ano} = 0.1$).

case with a low-porosity anode. Other conditions were the same as those shown in Fig. 4.8. The active reaction zone in which the charge transfer reaction proceeds was distributed unevenly in one side ($y \sim 500$ μm) while the local charge transfer current was concentrated into this side. The vertical part was not effectively used either. The active side was closer to the anode surface and so the anode gas transport was relatively better than that of the other side ($y \sim 600$ μm). This figure indicates that less than half of the electrode–electrolyte interface region was active in this case.

Figure 4.13 shows the characteristics of *i-V* and *i-P* for this case, along with the results for a flat cell. The porosity of the anode is 0.1 for the flat case also. The *i-V* characteristics clearly indicate the maximum current density due to the concentration overpotential at the high current density. Greater performance enhancement of the corrugated cell than the flat cell was not observed under this condition. Hence, the corrugated mesoscale structure is not useful in this case. The effect of the concentration overpotential needs to be carefully examined for designing an effective corrugated shape.
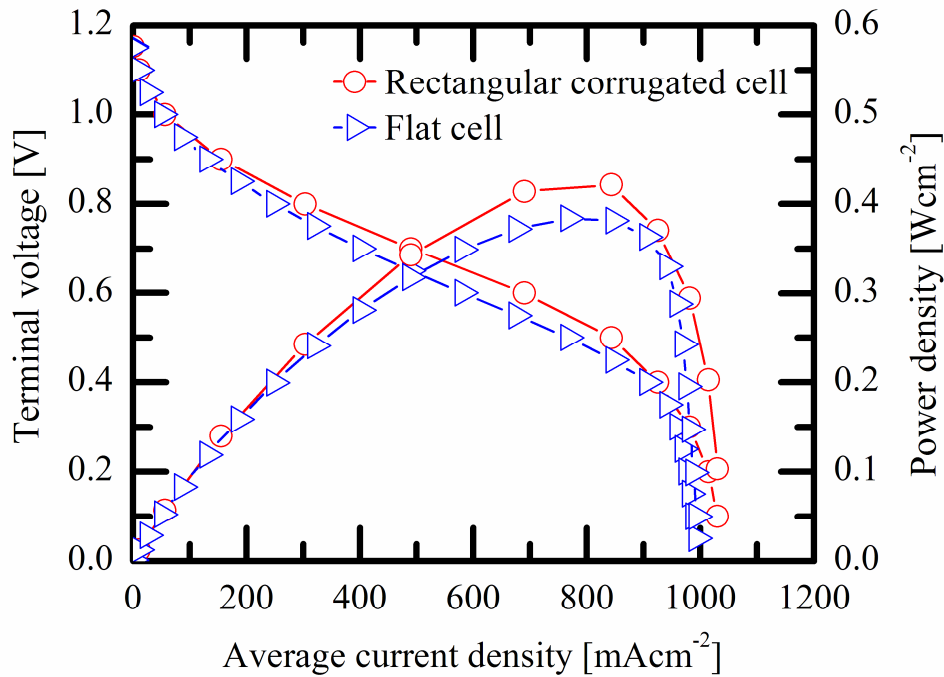

Fig. 4.13 Characteristics of *i-V* and *i-P* under low anode porosity condition ($\varepsilon_{ano} = 0.1$).

4.3 Summary

A two-dimensional numerical simulation was performed to understand the effect of corrugated-mesoscale structure control in an anode-supported cell containing a thin electrolyte on power generation performance. A flat-cell case in addition to six cases of the corrugated mesoscale structure with different interface area enlargement factors were calculated. We reported the following results.

(1) The mesoscale-corrugated cell enhanced the power generation performance compared to the flat cell because the local ionic current around the electrolyte was reduced due to interface enlargement. From the viewpoint of the representing mean voltage losses, the mean ohmic loss by ion transport and the mean activation overpotential of both electrodes decreased with increasing interface area enlargement. This was a result of the reduced local ionic current.

(2) The active reaction zone was distributed in the electrodes up to 10 μm from the electrode–electrolyte interface under the conditions in this study, and it strongly depends on the electric potential distribution of the ion-conducting phase.

(3) The degree of enhancement was closely related to the interface area enlargement factor of the corrugated cell. There existed a maximum value of the average current density enhancement for each case because the effect of the concentration overpotential increases with the increasing current density and electrode depths.

(4) For a low anode porosity case, the corrugated electrolyte shape did not enhance the cell performance and the maximum current density was observed at a high current density owing to the increasing concentration overpotential. Hence, it should be noted that anode porosity unfavourably affects enhancement by interface area enlargement if the anode porosity is extremely low.

Reference

[1] J.H. Nam, D.H. Jeon, "A comprehensive micro-scale model for transport and reaction in intermediate temperature solid oxide fuel cells", Electrochimica Acta 51 (2006) 3446-3460.

[2] P. Costamagna, P. Costa, V. Antonucci, "Micro-modelling of solid oxide fuel cell electrodes", Electrochimica Acta 43 (3-4) (1998) 375-394.

[3] E.A. Mason, A.P. Malinauskas, R.B. Evans III, "Flow and diffusion of gases in porous media", The Journal of Chemical Physics 46 (8) (1967) 3199-3216.

[4] D. Arnošt, P. Schneider, "Dynamic transport of multicomponent mixture of gases in porous solids", The Chemical Engineering Journal 51 (1995) 91-99.

[5] B. de Boer, "SOFC anode: hydrogen oxidation at porous nickel and nickel/yttria-stabilised zirconia cermet electrodes", Ph.D Thesis, University of Twente, Netherlands (1998).

[6] Y. Suzue, N. Shikazono, N. Kasagi, "Micro modeling of solid oxide fuel cell anode based on stochastic reconstruction", Journal of Power Sources 184 (2008) 52-59.

[7] R. Radhakrishnan, A.V. Virkar, S.C. Singhal, "Estimation of charge-transfer resistivity of $La_{0.8}Sr_{0.2}MnO_3$ cathode on $Y_{0.16}Zr_{0.84}O_2$ electrolyte using patterned electrodes", Journal of the Electrochemical Society 152 (1) (2005) 210-218.

Chapter 5
Conclusions

5.1 Conclusions

Chapter 2 discussed the active reaction zone of the porous electrode in SOFC. The characteristic lengths of electron, ion and gas transports were introduced and a scale analysis was performed based on these characteristic lengths assuming conventional electrode materials. From the scale analysis, the ion-conducting length was shortest among the three characteristic lengths; hence ion transport determines the active reaction zone under typical operating conditions. The electron-conducting length was sufficiently long in a conventional electrode. The gas-diffusion length was nearly equal to the ion-conducting length when the operating temperature is high and gas diffusivity is low; therefore, the active reaction zone is affected by the gas transport in this condition.

Chapter 2 presented the results of one-dimensional numerical simulation of the electrode. In case gas-diffusion length is sufficiently long, the active reaction zone was distributed close to the electrode–electrolyte interface. On the other hand, when the ion-conducting length is relatively short and is in the order of 10 μm, the effective thickness was linearly proportional to the ion-conducting length. The expansion of the effective thickness was observed in case

which the ion-conducting and gas-diffusion lengths are short because of the increasing concentration overpotential near the electrode–electrolyte interface. In this case, the portion of the ion current that is forced to move a long distance from the interface increases. Decreasing gas-diffusion length leads to increasing concentration overpotential and the ohmic loss due to ion conduction in the electrode. The scale analysis could not predict an accurate active reaction zone but it was confirmed that the predicted active reaction zone by scale analysis agrees with the results of the one-dimensional numerical simulation in the case of longer gas-diffusion lengths. The scale analysis is useful for intuitively understanding the effect of the transport phenomena in the SOFC electrode. A numerical simulation could clarify the effect of electron, ion and gas transport in the electrode on the active reaction zone and electrode performance.

Chapter 3 presented the results of the two-dimensional numerical simulation and power generation experiment of the SOFC with mesoscale-grooved structure on the anode side. From the simulation results, it was confirmed that the mesoscale-grooved structure enhances power generation performance when the groove size is sufficiently longer than the effective thickness of the electrode. Cell performance increased with increasing interface area enlargement. The electrochemical reaction occurred at the zone near to the electrode–electrolyte interface and the grooved bottom, in case of the mesoscale-grooved cell in particular. From the results of the experiment, the grooved cell also enhanced cell performance compared to the flat cell. The qualitative agreement of the interface area enlargement effect between simulation and experiment is confirmed. Moreover, it was confirmed from the impedance measurement that the reaction resistance was reduced by the mesoscale-grooved structure.

Chapter 4 discussed the effects of the corrugated-mesoscale structure control in the anode-supported cell containing a thin electrolyte on the power generation performance from the results of the two-dimensional numerical simulation. It was confirmed that the

mesoscale-corrugated cell enhances power generation performance compared to the flat cell. The representing mean voltage losses of ohmic loss by ion conduction and activation overpotential of both electrodes were reduced by the corrugated structure; they decreased with increasing interface area enlargement. The active electrochemical reaction zone was distributed at near the electrode–electrolyte interface, and it strongly depended on the electric potential distribution of the ion-conducting phase. Because the effect of the concentration overpotential increased with increasing current density and electrode depths, average current density enhancement had a maximum value. In the low anode porosity case, the corrugated cell did not enhance cell performance. The cell terminal voltage suddenly decreased with increasing current density at high current density owing to the increasing concentration overpotential.

5.2 Suggestions for future works

In this thesis, one-dimensional numerical simulation and scale analysis were examined for understandings the active reaction zone of the SOFC electrode. The effects of transport phenomena in the SOFC electrode on electrode performance were clarified. Further development of "direct" simulation in the electrode microstructure and a comparison between "direct" and macroscopic simulations are desired. Currently, measurement and quantification of a three-dimensional microstructure of the porous electrode and its correlation to electrode performance have been frequently investigated. The electrode microstructure, which is strongly related to the dimension of the three-phase boundary, influences the active reaction zone through the reactivity in the electrode. Therefore, a consideration of the effects of actual three-dimensional microstructure on the reaction zone must be investigated in future studies.

This thesis has investigated the possibility of mesoscale-structure control of the electrode–electrolyte interface in SOFCs. This possibility and its effectiveness were confirmed. It is suggested that the length of mesoscale structure is equal or longer than the "effective

thickness". It is possible to apply the mesoscale-structure control to other cell materials. The effectiveness of the mesoscale structure is highly sensitive to the concentration overpotential when the current density is relatively high and the size of the structure is large. Therefore, gas diffusivity of the porous electrode must be focused. Further investigations of mesoscale interface modification are desirable.

Nomenclature

ASR	area specific resistance	$\Omega\,m^2$
Bi	Biot number	
Bi_{FC}	fuel cell Biot number	
D_{ij}	binary diffusivity	$m^2\,s^{-1}$
$D_{i,K}$	Knudsen diffusivity of chemical component i	$m^2\,s^{-1}$
d	diameter	m
E	electric potential difference	V
E^{eq}	equilibrium electrode potential	V
E_0^{eq}	equilibrium electrode potential at standard state	V
E_0	EMF at standard state	V
F	Faraday constant	$C\,mol^{-1}$
I	current	A
i	current density	$A\,m^{-2}$
i_0	exchange current density	$A\,m^{-2}, A\,m^{-3}$
i_0^L	exchange current per TPB length	$A\,m^{-1}$
i_{tpb}^L	current per TPB length	$A\,m^{-1}$
i_{ct}	volume-specific charge transfer current	$A\,m^{-3}$
K	permeability	m^2
k_K	Kozeny constant	
l	characteristic length, thickness or height	m
l_{eff}	effective thickness	m
l_{th}	electrode thickness	m
L_{tpb}	TPB length	m
l_{tpb}	TPB density	m^{-2}
M	molecular weight	$kg\,mol^{-1}$

N	molar flux	$\text{mol m}^{-2}\,\text{s}^{-1}$
P	pressure or partial pressure	Pa
p	percolation probability	
R_{ct}	charge-transfer resistance	Ω
r^L_{ct}	charge-transfer resistance per TPB length	$\Omega\,\text{m}^{-1}$
R_0	universal gas constant	$\text{J mol}^{-1}\,\text{K}^{-1}$
S	surface area	m^2
s	molar production or consumption rate	$\text{mol m}^{-3}\,\text{s}^{-1}$
T	temperature	K
V	volume of computational domain	
v	volume fraction	
V_s	volume of solid phase	m^3
W	width	m
w	width	m
X	molar fraction	

Greek symbols

α	heat-transfer coefficient	$\text{W m}^{-2}\,\text{K}^{-1}$
β	transfer coefficient	
α_{area}	interface area enlargement factor	
ε	porosity	
η	overpotential	V
η_{cell}	total cell overpotential	V
λ	thermal conductivity	$\text{W m}^{-1}\,\text{K}^{-1}$
μ	viscosity	Pa s
σ	conductivity	S m^{-1}
τ	tortuosity factor	
Φ	electric potential	V

ϕ	electric potential	V
ϕ_0	Nernst potential	V
ϕ_{FC}	cell terminal voltage	V

Subscripts

act	activation
amp	amplitude
ano	anode
ave	average
bulk	bulk fluid
cath	cathode
ct	charge transfer
con	concentration
el	electron-conducting phase
ele	electrolyte
gas	gas diffusion
h	hydraulic
int	electrode–electrolyte interface
io	ion-conducting phase
meso	mesoscale structure
MOLB	mono-block layer built
ohm	ohmic
p	pore
per	period
ref	reference
s	solid plate
t	total
tpb	three-phase boundary

Superscripts

eff	effective value
eq	equilibrium
L	per unit length
m	mean value
0	bulk material